OMVPE GROWTH AND CHARACTERIZATION OF CARBON DOPED InAs

by

Simin Bagheri Najmi

B.Sc., Sharif University of Technology, 1997

M.Sc., University of Tehran, 2000

A THESIS SUBMITTED IN PARTIAL FULFILLMENT
OF THE REQUIREMENTS FOR THE DEGREE OF
DOCTOR OF PHILOSOPHY
in the Department
of
Physics

SIMON FRASER UNIVERSITY
Summer 2008

APPROVAL

Name: Simin Bagheri Najmi

Degree: Doctor of Philosophy

Title of thesis: OMVPE growth and characterization of carbon doped InAs

Examining Committee:

Dr. Karen Kavanagh
Professor, Department of Physics, SFU
Chair

Dr. Simon Watkins, Senior Supervisor
Professor, Department of Physics, SFU

Dr. Mike Thewalt, Supervisor
Professor, Department of Physics, SFU

Dr. Patricia Mooney, Supervisor
Professor, Department of Physics, SFU

Dr. Michael Chen, Examiner
Lecturer, Department of Physics, SFU

Dr. Matthew McCluskey, External Examiner
Professor, Department of Physics and Astronomy
Washington State University

Date Approved: June 20, 2008

Abstract

Carbon-doped InAs samples grown by organometallic vapor phase epitaxy were studied by Raman and IR spectroscopy. Local vibrational modes (LVMs) related to isolated substitutional carbon acceptors, carbon acceptor-hydrogen complexes, and dicarbon centers were detected in samples doped with two isotopes of carbon. Energies of the observed carbon-hydrogen modes are in close agreement with carbon acceptor-hydrogen modes in GaAs and InP, and are consistent with hydrogen occupying a bond-center position in the complex. No sign of substitutional carbon donors was observed. N-type conductivity of carbon-doped InAs was explained by the presence of dicarbon centers that are believed to be deep donors. The stretch mode of this complex was detected at 1832 cm^{-1} by Raman spectroscopy in as-grown and annealed samples. Annealing measurements performed on heavily carbon-doped InAs samples confirmed that the n-type conductivity observed for this material is due to the formation of dicarbon defects. The structural, electrical, and optical properties of n-type carbon-doped InAs samples annealed at temperatures of 400 °C and higher were studied using Raman and infrared spectroscopy, and X-ray diffraction. Based on the expected energy level of dicarbon donors in GaAs, we predicted that the dicarbon defects in InAs should introduce a resonant level close to or slightly above the conduction band minimum.

Keywords: InAs; carbon; OMVPE; semiconductors; vibrational-spectroscopy
Subject Terms: semiconductors; InAs; OMVPE; carbon

Acknowledgments

I would like to thank my senior supervisor, Professor Simon Watkins, for his invaluable guidance and support during this research. The completion of this thesis would not have been possible without his patience and encouragement.

I am thankful to the members of my supervisory committee, Dr. Mike Thewalt, Dr. Patricia Mooney, and Dr. Colombo Bolognesi for their guidance and feedback throughout my research. Special thanks to Dr. Thewalt, Michael Steger, and Albion Yang for obtaining the Infrared spectra. I am grateful to Dr. Micheal Chen for the use of his laboratory and providing great help during the Raman measurements. I would like to acknowledge the assistance of Dr. G. Soerensen in preparation of Hall samples. I am thankful to our group members Dr. Pitts, Dr. Zhang, Dr. Rao, and Dr. Jiang for their assistance with OMVPE growths and AFM measurements.

I would like to acknowledge Simon Fraser University, Department of Physics and National Science and Engineering Research Council of Canada (NSERC) for the financial support.

I would like to thank all my friends for the joyful hikes, lovely evenings, and all their support during these years. I am grateful to my family and my husband's for their support and encouragement throughout the years. Without each one of them, I could not have even dreamed about being at this point in my life. I can not thank my husband, Shahram, enough for his love and continuous support during this period. He has been my English teacher, ski instructor, and my best friend.

Contents

List of Tables

List of Figures

List of Abbreviations

CBE	chemical beam epitaxy
CBr_4	carbon tetrabromide
CCD	charge coupled devices
CCl_4	carbon tetrachloride
DLTS	deep level transient spectroscopy
FTIR	Fourier transform IR
HBT	heterojunction bipolar transistor
HRXRD	high resolution X-ray diffraction
IR	infrared
LO	longitudinal optical
LVM	local vibrational mode
MBE	molecular beam epitaxy
MFC	mass flow controller
MOMBE	metal organic molecular beam epitaxy
OMVPE	organometallic vapor phase epitaxy

PLP	plasmon-LO-phonon
SIMS	secondary ion mass spectroscopy
TBAs	tertiarybutylarsine
TBP	tertiarybutylphosphine
TEGa	triethylgallium
TEM	transmission electron microscopy
TMIn	trimethylindium
TMSb	trimethylantimony
TO	transverse optical
XRD	X-ray diffraction

Chapter 1

Introduction

Impurities in III-V semiconductors have played an important role in the progress of semiconductor technology. Therefore, extensive theoretical and experimental research has been required to investigate the properties of impurities in III-Vs such as their electronic structure, vibrational properties, concentration and profile, formation energies, and diffusion properties.

Impurity atoms can be introduced intentionally into semiconductors by a process called doping. Dopant atoms incorporate in the crystal structure by replacing lattice sites of the host atoms (substitutional impurities) or occupying the sites between the host atoms (interstitial impurities). Depending on the occupied lattice sites (group III or group V host atoms), they become donors or acceptors and give rise to n-type or p-type conductivity, respectively. The introduction of impurities not only changes the electrical properties of semiconductors, but also modifies their structural and vibrational characteristics. By studying these changes, it is possible to determine the properties of dopants such as their concentration, and the occupied lattice site.

The careful selection of dopant atoms is crucial to achieve the desired properties in semiconductor materials. These atoms need to be highly soluble in the host crystal, have low diffusivity to provide precise doping profiles, have high electrical activation, and high thermal stability. Among the p-type dopants such as Be and Zn, carbon has proven to have the most of these qualifications. High doping levels can be achieved with Be and Zn, which substitute for the group III sublattice to produce p-type

material. Be is highly toxic however, and Zn has a large diffusivity which is undesirable for certain applications. In principle carbon, as a group IV element, might be expected to occupy either the group III or group V sublattice. However, local vibrational mode studies have proven that carbon normally occupies the group V lattice sites in most semiconductors such as GaAs, GaSb, and AlAs and becomes an acceptor [1, 2, 3]. Doping levels as high as 10^{20} cm^{-3} can be easily achieved by carbon doping [4]. Although extensive research has been done on the properties of carbon in some materials such as GaAs and AlAs, very little is known about the characteristics of carbon-doped InAs and GaSb.

InAs is a direct gap semiconductor with a band gap of 0.35 eV at room temperature and zincblende crystal structure (figure 1.1). Having the lowest energy band gap after InSb of the III-V semiconductors, InAs has been of interest for applications in high speed electronics, infrared devices such as detectors and lasers, and integrated Hall sensors. It has also been of technological importance as a constituent of ternary and quaternary semiconductors such as InGaAs and InGaAsP.

InGaAs lattice matched to InP is a desirable base layer for InGaAs/InP heterojunction bipolar transistors (HBT). A highly p-type base layer with sharp interfaces is required in order to get high speed transistors. Although carbon is a good p-type dopant for most III-V structures because of its low diffusivity and high solubility, OMVPE-grown carbon-doped InGaAs lattice matched to InP is highly compensated. The hole concentration is relatively low and special growth conditions (such as low substrate temperature and V:III ratio) are needed to improve it [5]. This has been attributed to the amphoteric behavior of carbon in this material [6].

Carbon-doped InAs shows different characteristics than other carbon-doped III-Vs. The experimental reports of the properties of carbon-doped InAs have shown that it becomes n-type after doping [7, 8, 9]. It was assumed that carbon occupies the group III lattice sites in this material and becomes a donor [9]. However, theoretical calculations of the formation energies have shown that carbon on an In lattice site has a higher formation energy than carbon on an As lattice site. Therefore, carbon donors are less stable than carbon acceptors [10]. To our knowledge, this contradictory situation has never been resolved. In this work, we have studied the characteristics of

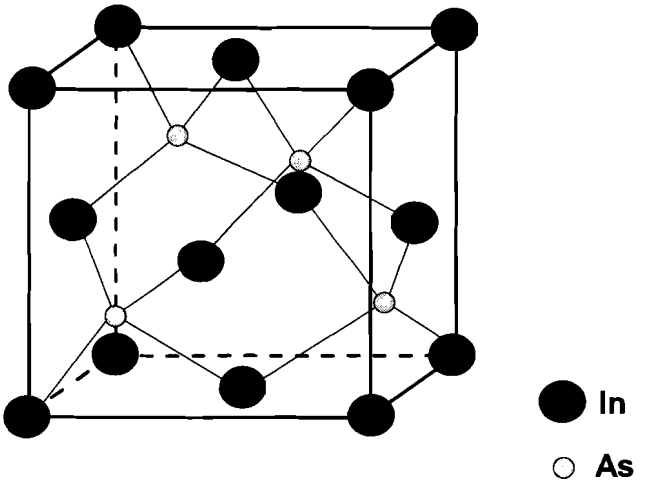

Figure 1.1: Unit cell of InAs with the zincblende structure.

carbon doped InAs samples grown by organometallic vapor phase epitaxy (OMVPE). The effects of carbon doping on the electrical and structural properties of InAs have been studied using Hall measurements and X-ray diffraction (XRD). The lattice site of carbon atoms has been determined using the results of Raman and infrared (IR) spectroscopy methods. Hydrogen passivation of carbon impurities has been studied and the origin of the n-type conductivity of carbon-doped InAs samples has been identified. The thermal stability of carbon dopants has been investigated by annealing the samples at different temperatures and ambients and the resultant changes have been studied by different characterization methods.

GaSb is a direct gap semiconductor with a room temperature band gap of 0.725 eV and having the zincblende crystal structure. Carbon doping of GaSb has previously been studied by our group. Local vibrational modes of isolated carbon atoms have been detected by Raman spectroscopy [2] and the structural effects of carbon on GaSb have been studied by Watkins *et al.* [11]. Hole concentrations higher than 10^{19}cm^{-3} can be easily achieved by carbon doping. There has been no evidence of hydrogen passivation of carbon impurities in this material. In this thesis, we report

our results of Raman and IR spectroscopy measurements of carbon-doped GaSb. The lattice site of carbon impurities has been confirmed using the isotopic shift of the local vibrational mode (LVM) of carbon. IR reflection and absorption measurements have been conducted on GaSb:C samples grown at different substrate temperatures to search for evidence of carbon-hydrogen complexes.

The remaining chapters of this thesis are dedicated to the results of the above-mentioned studies. In chapter two, the experimental methods used in this work are introduced and the theory behind each measurement method is explained briefly. In chapter three, carbon doping of InAs grown by OMVPE is discussed and some growth issues such as the effects of the substrate temperature on the doping efficiency are presented. The electrical, structural, and vibrational characteristics of carbon-doped InAs investigated by different methods are discussed. It is followed by a conclusion about the lattice site of carbon in InAs and an explanation for the n-type conductivity of InAs:C. The effects of annealing on the properties of carbon doped InAs samples are described in chapter four. More evidence is introduced to confirm the origin of n-type conductivity of carbon-doped InAs. Chapter four contains a short discussion about carbon doping of GaSb and the results of our search for evidence of hydrogen passivation of carbon acceptors in this material. Chapter five concludes the thesis by summarizing all the results and future research possibilities.

Chapter 2

Experimental methods

In this chapter we outline the experimental methods that were used to produce and characterize the materials of this work. For each method a brief explanation of the instrument has been provided. The theory behind the spectroscopy methods (Raman and infrared spectroscopy) and their applications in studying semiconductor materials have been explained in more detail.

2.1 Organometallic vapor phase epitaxy

OMVPE is one of the most widely-used methods in the epitaxial growth of thin semiconductor layers both for scientific and industrial purposes. It is based on the thermal decomposition of the precursors (organometallic compounds or hydrides) in the vicinity of a heated substrate and the incorporation of the released atoms in the growing layer. An inert gas such as high purity hydrogen or nitrogen is used to carry the precursors from their bubblers to the reactor chamber.

Figure 2.1 shows a simplified diagram of the Thomas Swan OMVPE system used to grow the materials for this study. High purity hydrogen gas transfers the group III and group V precursors from the bubblers to the vertical reactor through separate lines. This prevents mixing and possible reaction of the precursors before entering the reactor. A valve manifold can switch the mix of precursor and hydrogen gas between the run and the vent lines, directing the gas to the reactor and the scrubber,

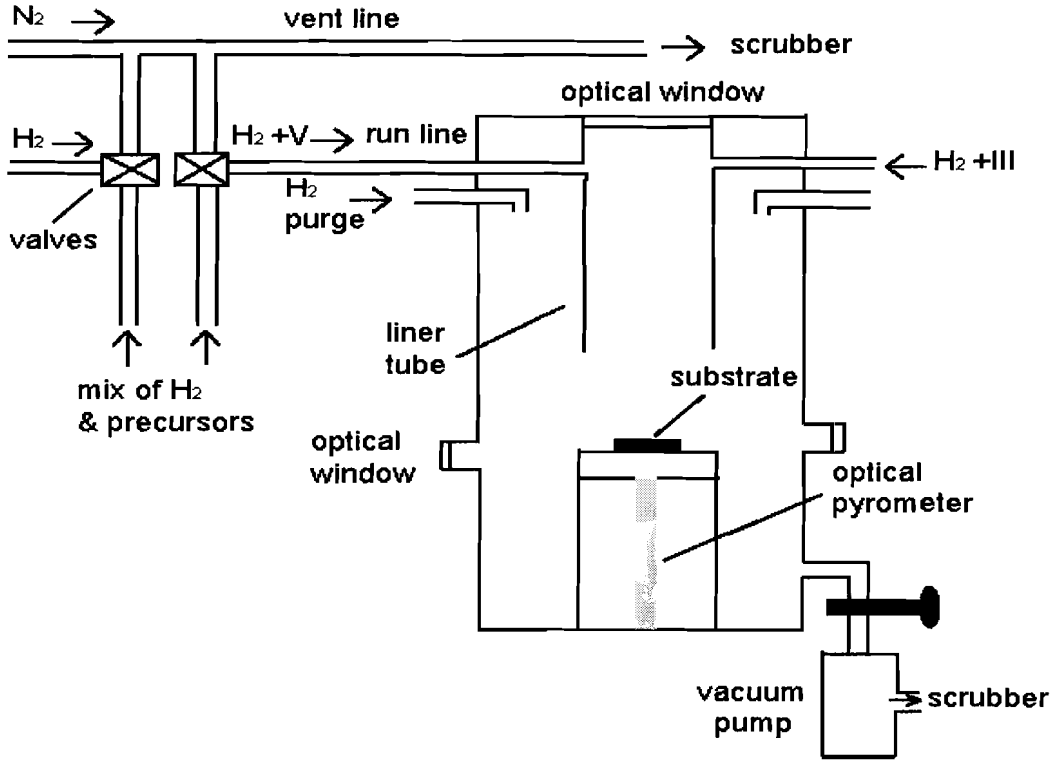

Figure 2.1: A schematic view of OMVPE system.

respectively. The reactor pressure is lowered down to 50 Torr using a vacuum pump.

Inside the reactor, the gaseous mixture flows downwards toward the substrate which lies on a graphite susceptor. The susceptor temperature is raised to the desired growth temperature by an electrical resistance heater placed at the backside of the susceptor and is controlled by feedback from an optical pyrometer which also monitors the backside of the susceptor.

The gas flow inside the reactor is one of the parameters that determine the uniformity of the grown layers; however, the ideal case of having a steady laminar flow is hard to achieve. In fact the hydrodynamics of gas flow is one of the most complex aspects of the OMVPE system because it can be influenced by many factors such as reactor configuration, pressure, and thermal convention. A general overview of the gas dynamics can be found in Stringfellow's book [12]; however, detailed treatment of this problem requires complicated computer simulations.

2.1.1 Precursor delivery

Materials used as OMVPE precursors are either organometallic molecules or gaseous materials such as carbon tetrachloride (CCl_4) and H_2S. The organometallic materials are mostly in liquid form (except for solid Trimethylindium (TMIn) and carbon tetrabromide (CBr_4)) and are stored in stainless steel bubblers kept in ethylene glycol baths in order to control their temperature (figure 2.2).

Using a stainless steel inlet pipe, hydrogen is forced into the bubbler where it forms bubbles saturated with precursor molecules. The vapor mixture of hydrogen and precursor molecules is then carried towards the growth system by an outlet pipe. The precursor flow rate (f_p) depends on the partial pressure of the precursor inside the bubbler and can be calculated by the following equation based on the ideal gas law:

$$f_p = \frac{F_H}{22407.47} \frac{P_V(T)}{P_B - P_V(T)} \quad mol/min \tag{2.1}$$

where F_H is the volume flow rate of hydrogen at standard temperature and pressure (cm^3/min), and $P_V(T)$ and P_B are the precursor vapor pressure and bubbler pressure, respectively. The flow rate of hydrogen is determined by a mass flow controller (MFC) installed on the inlet port of each bubbler and the bubbler pressure is controlled by an electronic pressure controller. The vapor pressure of the precursors depends on the temperature and two other empirical parameters (a, b) that are characteristic of each material [12]:

$$P_V(T) = 10^{a-b/T} \quad (Torr) \tag{2.2}$$

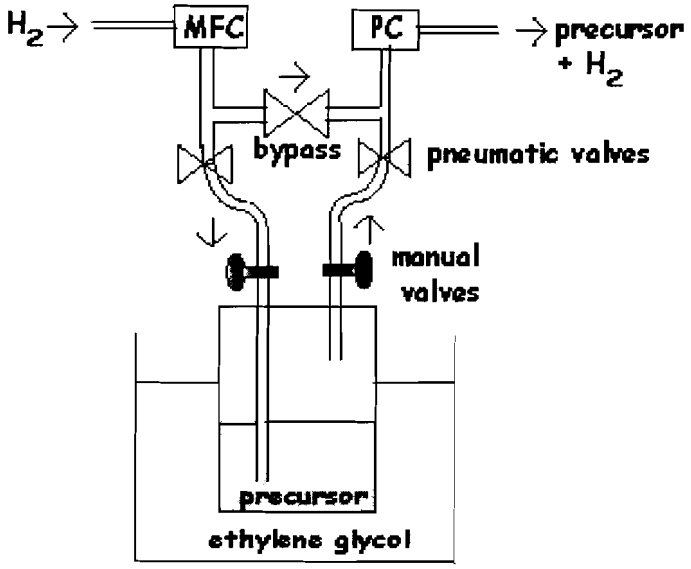

Figure 2.2: A schematic view of precursor bubbler. MFC and PC refer to mass flow controller and pressure controller, respectively.

Table 2.1 summarizes all of the precursors used for this study together with their physical properties.

Table 2.1: A summary of physical properties of precursors used in this study.

Precursor	MP (°C)	BP (°C)	a	b (K)	T (°C)
tertiaybutylarsine (TBAs)	-1	69	7.243	1509	4
trimethylindium (TMIn)	88	135.8	10.520	3014	18
triethylgallium (TEGa)	-82.5	143	9.172	2532	18
trimethylantimony(TMSb)	-87.6	80.6	7.707	1697	4

2.1.2 Pyrolysis of precursors

As mentioned before, the mixture of hydrogen and precursors arrives at the reactor and moves downwards toward the heated substrate. The velocity of the gas flow decreases in the vicinity of the susceptor and becomes zero when it impinges on the substrate. The space where the retardation of gas flow happens is called the *boundary layer*. The organic molecules undergo thermal decomposition in this layer or on the solid surface due to the high temperature of the substrate.

There are two kinds of reactions that happen during the OMVPE growth process: homogeneous reactions that take place in the gas phase in the boundary layer and heterogeneous reactions that occur at the solid surface. Two main types of homogeneous reactions are simple homolysis and β-hydride elimination. The first one which is common for the $M(CH_3)$ molecules produces methyl radicals and the latter results in the production of alkenes and molecules with M-H bonds. Figure 2.3 shows examples for each kind of these reactions.

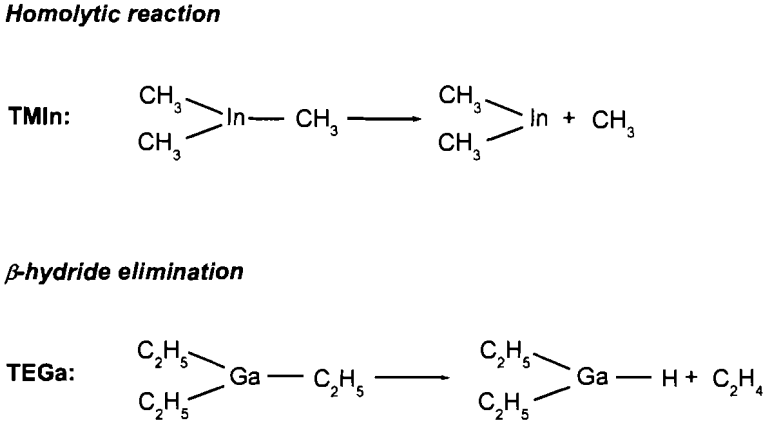

Figure 2.3: Samples of homolytic and β-hydride elimination reactions.

The pyrolysis reactions for different precursors have been discussed in detail by Stringfellow [12]; here we briefly explain the pyrolysis of TMIn and TBAs that were

mostly used in this work. The decomposition of TMIn happens through a homolysis reaction. Due to the relatively low In-methyl bond strength (47 kcal/mol), the homolysis occurs at temperatures as low as 300 °C. The rate of decomposition increases rapidly with temperature and at $\sim$ 350 °C it is 100 % decomposed. The following equations show the related chain reactions.

$$In(CH_3)_3 \rightarrow In(CH_3)_2 + CH_3 \tag{2.3}$$

$$In(CH_3)_2 \rightarrow In(CH_3) + CH_3 \tag{2.4}$$

$$In(CH_3) \rightarrow In + CH_3 \tag{2.5}$$

The pyrolysis of TBAs is more complicated. There are different possible reactions including homolysis and β-hydride elimination that can lead to the decomposition of this material. Because of the weak bonding between C and As in the t-butyl radical, the pyrolysis happens at fairly low temperatures.

2.1.3 Formation of epitaxial layers

The interface of the boundary layer and the substrate is not in thermodynamic equilibrium due to the high concentration of the species produced from thermal decomposition of the precursors in the gas phase. Such a system tends to restore the equilibrium by reducing the difference between the chemical potentials of the gas phase (μ_g) and the solid phase (μ_g):

$$\Delta\mu = \mu_g - \mu_s \tag{2.6}$$

Although the growth rate of the layer is mainly determined by thermodynamics, it is influenced by other parameters such as mass transport via diffusion through the boundary layer and also the diffusion of adatoms on the surface. Figure 2.4 shows a schematic view of the surface processes that are involved in the formation of the thin film. The first step is the adsorption of the species produced from the decomposition of the precursors, at the surface. Species are first physisorbed which means they bind to the surface by weak Van der Waals forces. At this stage they either desorb from the surface (due to their thermal energy and the weak bonding to the surface) or migrate to find a site where they can form multiple chemical bonds and become chemisorbed.

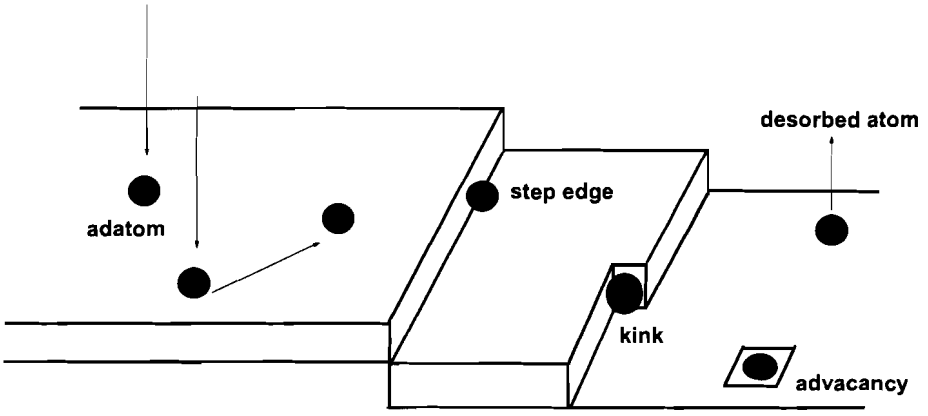

Figure 2.4: A schematic view of the processes happening at the surface.

It is known that the surface of the macroscopically flat substrates includes imperfections such as steps, kinks, and vacancies. These are the low energy positions of the surface that act as the preferred adsorption sites. The adatoms diffuse across the surface to find a low energy site such as a step edge and get incorporated in the growing crystal. Since the substrates used for OMVPE growth are slightly misscut from a low index plane typically (001), their surface includes monoatomic steps with terraces and edges. If the substrate temperature is high enough or the flux of constituents is low, the adatoms have enough mobility to diffuse on the surface and get incorporated on the step edges. The epitaxial layer forms by the movement of the step edges along the terraces. This is called step-flow growth [13].

OMVPE growth is usually conducted under high group V partial pressures (higher V:III ratios) to prevent degradation of the surface due to the desorption of these volatile atoms. Therefore the growth rate is mostly controlled by the supply of the group III atoms. At low growth temperatures, the growth rate is determined by the decomposition rate of the group III precursors. Therefore it increases by raising the growth temperature. At intermediate growth temperature (550 °C $<$ T $<$ 750 °C), the growth rate is almost temperature independent because the pyrolysis of

the precursors is complete and growth rate is diffusion limited (gas diffusion depends weakly on temperature). At very high substrate temperatures the desorption of group III atoms from the surface may decrease the growth rate.

2.2 High resolution X-ray diffraction

High resolution X-ray diffraction (HRXRD) was used to determine the structural properties of the layers in this work. Computer simulation of the obtained diffraction patterns, so called "rocking curves", provided information about the composition and the thickness of the epitaxial layers.

2.2.1 X-ray diffractometer

The instrument that was used in this work is a Bede D3 triple axis diffractometer and consists of an X-ray source, beam conditioner, sample holder, and a detector. Figure 2.5 shows a schematic view of the apparatus. The X-ray source is a vacuum tube in which electrons emitted from the cathode hit the copper target placed at the anode. The excitation of the electrons from the ground state to higher energy levels creates vacancies in this state. Electrons from higher energy levels fall down to the ground state to fill these vacancies and their energy releases as X-rays. The X-rays produced by transitions from the n=2 level to n=1 level are called Kα rays with the wavelength of 1.514 Å. The voltage and the current used to operate the source were 40 KV and 30 mA, respectively.

The beam conditioner consists of two silicon crystals with channels cut inside them and oriented in such a way that (220) diffracted beams are transmitted. The combination is used to both collimate the X-ray beam and make it monochromatic. The beam can either be reflected symmetrically through the channels that are parallel to the diffracting planes (path (2) in figure 2.5) or asymmetrically through the other channels (path (1) in figure 2.5). The first set of channels (path 2) provides the highest possible resolution and the second one (path 1) is used to obtain high intensity. In this work asymmetrically cut channels were used to attain high intensity.

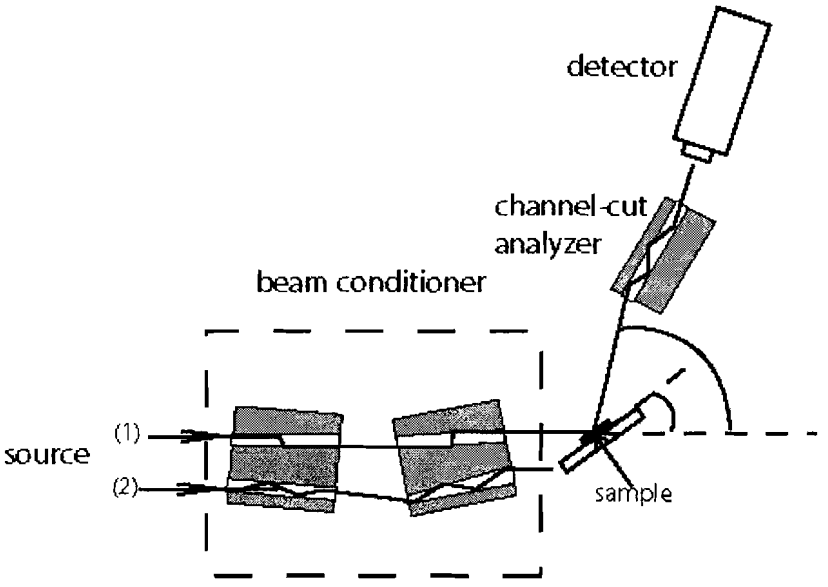

Figure 2.5: A schematic view of the XRD setup. X-rays are reflected asymmetrically through path (1) and symmetrically through path (2).

The sample is mounted on the holder using small pieces of wax in order to minimize the amount of external stress on the sample. The holder sits on a high precision stage so that it can be rotated to the desired angle. It can also rotate around the vertical and horizontal axes in the plane of the holder so that an exact orientation of the sample at the diffraction angle can be attained.

The detector is a combination of a scintillator and a photomultiplier tube. The scintillator converts the X-rays to low energy visible photons that are counted by the photomultiplier. A channel-cut analyzer crystal is placed between the sample and the detector and can be moved in and out of the diffracted beam. It is mostly used for reciprocal space mapping to narrow down the angular range of the beam entering the detector.

To measure the rocking curve of a layer, the sample holder and the detector are rotated to the Bragg angle (θ_B) and $2\theta_B$, respectively. A θ-2θ scan can be performed in any angular range around the Bragg angle.

2.2.2 Theory of X-ray diffraction

The scattering of X-rays in the crystal can be treated using two different theories: dynamical theory and kinematical theory. Dynamical theory provides a full solution of the wave equation inside the crystal by taking into account the diffraction and absorption of the waves as they propagate within the material. According to this model, the incident beam at each atomic layer becomes weaker as it travels inside the crystal due to the diffraction and absorption. Therefore, an extinction depth can be defined at which the amplitude of the incident beam becomes negligible. This theory is used by the Bede RADS software package that was used to simulate the rocking curves in this work. The explanation of this theory is beyond the scope of this work and can be found in many references such as [14].

In the kinematical theory, the attenuation of the wave inside the crystal is ignored. Therefore, the incident wave at each atomic layer is assumed to have the same amplitude. Also the deviation of the refractive index of the crystal from 1 is ignored and therefore the wavelength of the waves inside the crystal is assumed to be the vacuum value. In spite of the simplicity of the kinematical theory, it provides a good approximation in cases where the extinction length is large compared to the sample thickness.

The Bragg law can be used to explain the diffraction of the X-rays from the crystal. According to this law, the lattice spacing of a crystal can be calculated by the following equation:

$$2d_{hkl}.sin\theta_B = n\lambda \tag{2.7}$$

where d_{hkl} is the spacing between the lattice planes with Miller indices (hkl), θ_B is the Bragg angle, λ is the wavelength of the X-ray, and n is an integer. The diffraction is defined as symmetrical or asymmetrical if the diffracting planes are parallel or nonparallel with the crystal surface, respectively. Figure 2.6 shows the symmetrical diffraction of X-rays from lattice planes. The interference of two reflected beams is constructive if their path difference, $2d_{hkl}\ sin\theta_B$, is an integer multiple of the wavelength.

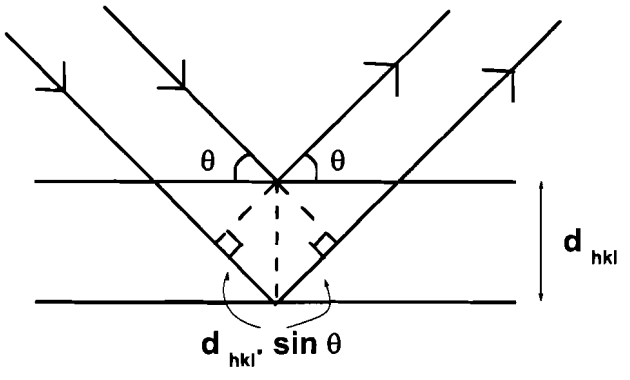

Figure 2.6: Diffraction of X-rays from the lattice planes with Miller indices (hkl).

2.2.3 Rocking curves of doped layers

The introduction of dopants in semiconductors usually results in a change of the lattice constant of the crystal due to two factors: the difference between the atomic radii of the dopant atoms and those of the replaced host atoms (size effect) and the presence of free charges. Considering only the size effect, if the covalent radius of the dopant atom is smaller (bigger) than that of the corresponding host atom, a lattice contraction (expansion) occurs. The amount of this contraction (expansion) is proportional to the difference between the atomic radii and also the concentration of the dopant atoms. The effect of free charges can be in the opposite sense to that of size effect and the overall lattice change depends on the ratio of these two effects [15]. The different lattice constants of the doped and the undoped material results in the appearance of two separate peaks in the rocking curve of the structure. The angular separation between these peaks can be used to determine the amount of strain in the layer.

As the thickness of the doped layer increases, the elastic energy increases. Beyond a critical value of thickness, stress becomes released by forming misfit dislocations which results in the formation of a partially relaxed layer (Figure 2.8). If the thickness of the doped layer is lower than this so-called critical thickness, the lattice constant

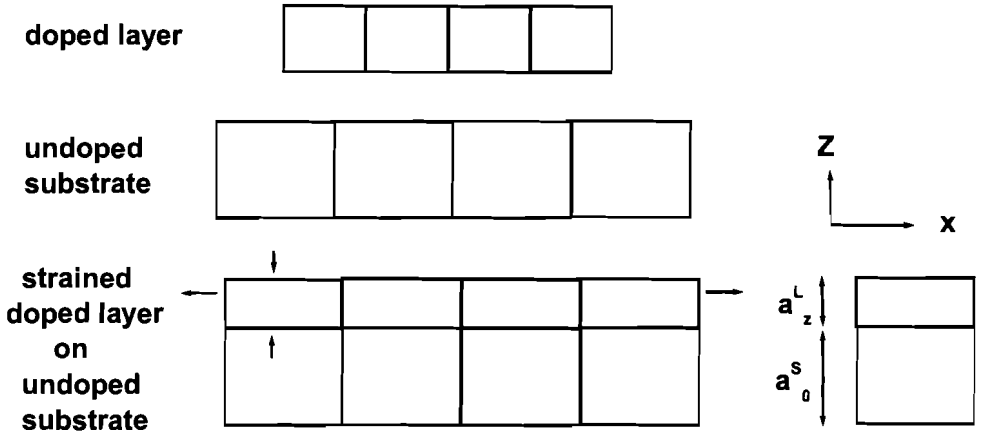

Figure 2.7: A schematic view of the epitaxial layer under biaxial tensile strain.

of the epilayer is modified in the growth direction due to strain.

Figure 2.7 shows the modification of the lattice constant for a coherent layer (thinner than critical thickness) grown on a substrate with a different lattice constant.

Since there is no force acting on the layer in growth direction, the component of stress in this direction is zero (σ_{zz}=0). The in-plane components of the strain tensor are equal due to equal components of stress in the plane of the growth (σ_{xx}=σ_{yy}). Components of strain tensor can be calculated as follows [16]:

$$\epsilon_{xx} = \epsilon_{yy} = \frac{a_0^S - a_0^L}{a_0^L} \tag{2.8}$$

$$\epsilon_{zz} = \frac{a_z^L - a_0^L}{a_0^L} \tag{2.9}$$

where $a^S{}_0$ is the lattice constant of the substrate (undoped material), $a^L{}_0$ is the unstrained lattice constant of the doped layer, and $a^L{}_z$ is the component of the lattice constant of the strained layer in the growth direction.

$a^L{}_z$ can be obtained using a symmetric X-ray diffraction measurement provided

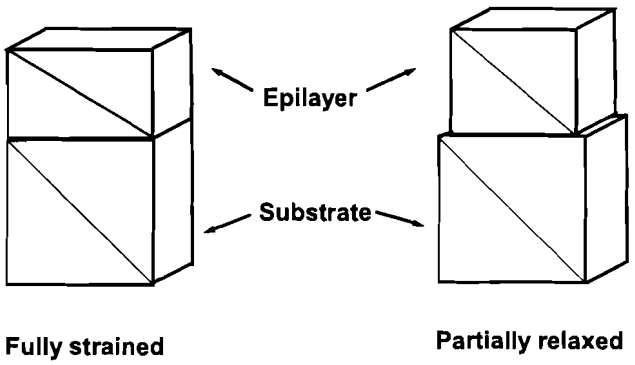

Figure 2.8: A schematic view of fully strained and partially strained epilayers on the undoped substrate.

that the lattice constant of the substrate (undoped material) is known:

$$(\frac{\Delta a}{a})_{\perp} = \frac{a_z^L - a_0^S}{a_0^S} = -\Delta\theta_B \cot\theta_B \tag{2.10}$$

The strained lattice constant is related to the unstrained one by the following equation:

$$a_0^L = \frac{C_{11}}{C_{11} + 2C_{12}}(a_z^L - a_0^S) + a_0^S \tag{2.11}$$

where C_{11} and C_{12} are the stiffness coefficients. As mentioned before, by making certain assumptions, the concentration of the dopant atoms can be deduced from the amount of change of the lattice constant.

2.3 Hall effect measurements

Electrical properties of InAs:C samples such as carrier concentration and mobility were measured by the Van de Pauw technique [17]. Electrical contacts were fabricated by forming In metal contacts on the corners of square samples, and annealed under nitrogen at $\sim$ 300°C for three minutes.

2.4 Infrared spectroscopy

Infrared (IR) spectroscopy is one of the most important methods of analyzing the vibrational properties of semiconductors. In this method, the frequency of the incident IR light is varied continuously and the reflectance or transmittance of the sample is measured as a function of the frequency. There are three regions of IR spectroscopy based on the spectral range of the incident light: far-IR (150-500 cm^{-1}), mid-IR (400-4000 cm^{-1}), and near-IR (3300-13300 cm^{-1}). In this work transmission measurements in the far-IR and mid-IR range were used to study the local vibrational modes of carbon and carbon-hydrogen complexes in semiconductors.

2.4.1 Theory of infrared spectroscopy

The simplest way to understand the interaction of light with material is using classical dispersion models [18]. In these models, material can be considered as an ensemble of harmonic oscillators. Each oscillator becomes polarized in response to external radiation where the amount of polarization is proportional to the intensity of the external electric field as:

$$\mathbf{p} = \hat{\alpha}\epsilon_0\mathbf{E} \tag{2.12}$$

where α is the electric polarizability of the material, $\mathbf{p}$ is the polarization vector, and $\mathbf{E}$ is the electric field of the external radiation. Although $\hat{\alpha}$ is a Hermitian tensor in general, for isotropic materials it reduces to a scalar which is called the dielectric function, because it only has identical diagonal elements.

The induced polarizability can be stated in terms of the parameters of a harmonic oscillator as:

$$\hat{\alpha} = \frac{e^{*2}}{\epsilon_0 m^*} \frac{1}{\omega_0^2 - \omega^2 + i\omega\gamma} \tag{2.13}$$

where e* and m* are the effective charge and reduced mass of the dipole, respectively, ω_0 is the resonance frequency, and γ is the damping coefficient of the oscillator. The electric polarization of the medium is defined as the sum of the polarizabilities of the particles in the unit volume:

$$\mathbf{P} = \sum \mathbf{p}_i = N\mathbf{p} \tag{2.14}$$

where N is the density of the particles. The dielectric function is related to the polarizability as:

$$\hat{\epsilon} = 1 + N\hat{\alpha} = 1 + \frac{\omega_p^2}{\omega_0^2 - \omega^2 + i\omega\gamma} \tag{2.15}$$

where

$$\omega_p = \sqrt{N\frac{e^{\star 2}}{\epsilon_0 m^*}} \tag{2.16}$$

is called the plasma frequency.

The dielectric function of a material is determined by different kinds of oscillators representing vibrations of valence electrons, free carriers, and lattice. In the IR spectral region, it can be assumed that only valence electrons contribute to the polarization because the core electrons are strongly bound and have no contribution to the dielectric function.

2.4.1.1 Free carriers

The contribution of free carriers to the dielectric function can be calculated using the Drude dielectric function:

$$\epsilon_{FC} = 1 + \frac{\omega_p^2}{i\gamma\omega - \omega^2} \tag{2.17}$$

where ω_p and γ are the plasma frequency and damping coefficient, respectively, and are related to the carrier concentration, effective mass of carriers, and their mobility.

2.4.1.2 Lattice vibrations

Atoms in a crystal oscillate around their equilibrium positions. The collective motion of atoms forms the lattice waves which can be expressed in terms of independent normal modes. Similar to light waves that are composed of photons, normal modes of lattice vibrations are quantized and this quantum is called a phonon. The frequency of phonons is related to their wavevector through a phonon dispersion relation.

Atoms can vibrate parallel or perpendicular to the direction of wave propagation and give rise to longitudinal (L) or transverse (T) modes, respectively. If the atoms in a primitive cell vibrate in phase with each other, they give rise to low energy acoustical mode phonons. The higher energy optical modes are the result of the

out of phase vibrations of these atoms. Therefore, the dispersion relation of crystals with one atom per unit cell includes only longitudinal acoustical (LA) and transverse acoustical (TA) branches; however, crystals with two atoms per unit cell such as zinc blende type crystals, have higher energy optical branches (LO and TO) as well. In general, for a crystal with N atoms per unit cell, there are 3 acoustical and 3N-3 optical branches. Figure 2.9 shows a typical dispersion diagram for a one dimensional crystal with two atoms per unit cell.

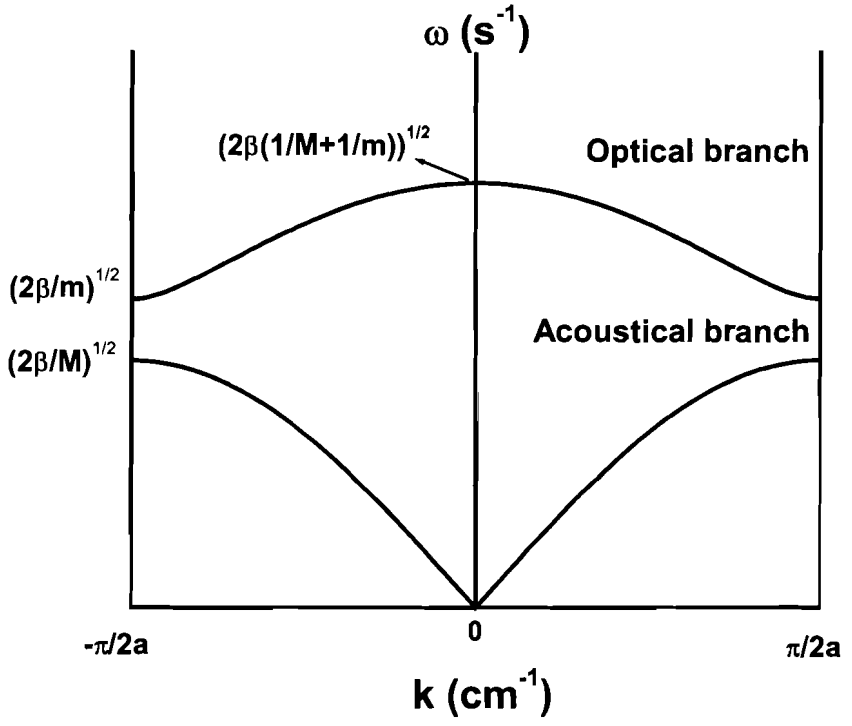

Figure 2.9: A typical phonon dispersion diagram for a one dimensional crystal with two atoms of masses m and M per unit cell. a is the lattice constant and β is the force constant.

The phonons whose frequencies lie inside the gap between the optical and acoustical branches are not allowed to propagate inside the crystal. The width of this

forbidden gap depends on the difference between masses of the two atoms. For example when the masses are equal, this width becomes zero at the zone boundaries.

Local vibrational modes (LVMs) The introduction of impurities into a semiconductor material not only breaks the symmetry of the crystal, but also affects its vibrational properties and leads to the occurrence of new vibrational modes. Studying these new modes can provide information about the properties of the defects. Several models have been developed to study the impurity-related vibrational modes such as linear chains of crystal atoms containing mass defects [19], Green's function treatment [20], and methods using ab initio calculations [21]. Although the sophisticated methods provide more accurate results, the simpler models give more intuitive pictures of impurity-related vibrational modes.

In this model, the compound semiconductor crystal is considered as a linear chain of diatomic unit cells where M and m are the masses of the heavy and the light atoms respectively and k is the force constant between the nearest neighbors. The vibrational modes of the impurity can be calculated by replacing one of the masses by the mass of the impurity atom and assuming that the force constant does not change.

Solving the simple harmonic equations assuming the periodic boundary conditions, one can calculate the frequencies of the LVMs [19].

Substitution of a host atom with an impurity can lead to several cases:

1. The lighter host atom of mass m is replaced by the impurity of mass m′:

   - if m′ <m, then a vibrational mode appears at a frequency higher than the lattice modes. This extra mode is highly localized around the impurity atom and does not propagate inside the lattice (local vibrational mode or LVM). Decreasing the mass of the impurity atom results in more localization of this mode.
   - if m′ >m, then there is a mode in the forbidden gap between the optical and acoustical modes of the lattice.

2. The heavier host atom of mass M is replaced by the impurity of mass M′:

- if M′ <M, then two new modes appear: one highly localized mode at a frequency higher than the lattice frequencies and another one inside the forbidden gap.
- if M′ >M, then there are no localized modes according to the chain model.

There are some differences between the gap modes and the LVMs. Although the gap modes are also localized in the vicinity of the impurity atoms, they involve considerable motion of the neighboring atoms as well. Also, decreasing the mass of the impurity atom does not result in more localization of the gap modes [22, 23]. Figure 2.10 shows the difference between vibrational amplitudes of the impurity and the host atoms in LVM and gap modes.

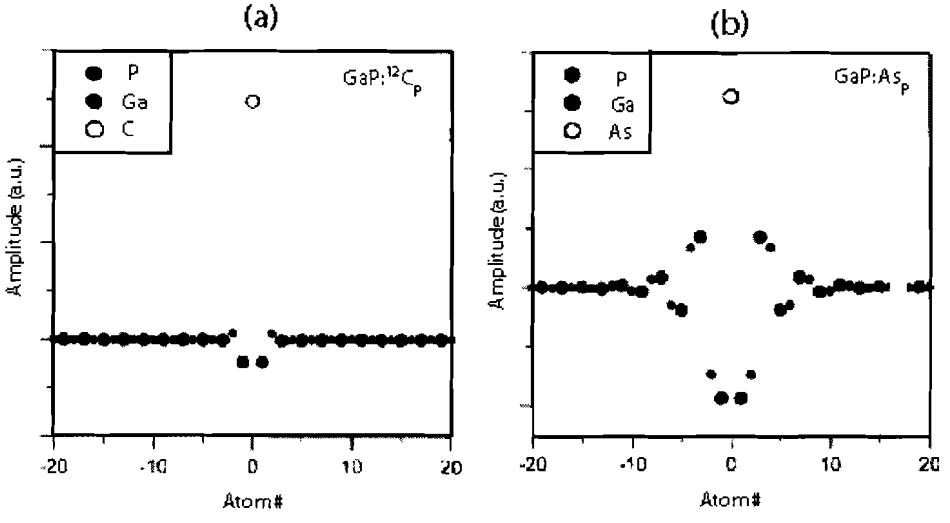

Figure 2.10: A comparison between vibrational amplitudes of the impurity and the host atoms in LVM and gap modes. a) LVM of carbon impurities in GaP, b) gap mode of the As impurities in GaP. (*J. Appl. Phys., Vol. 87, No. 8, p. 3593 (2000)*)

The frequency of local modes is very sensitive to the symmetry of the surrounding environment of the impurity. Replacing the impurity atom or the neighboring atoms

with their isotopes, results in shifts of LVM frequencies. The amount of this frequency shift can be used to determine the identity of the LVM and also the lattice site occupied by the impurity atom. The empirical diatomic model which assumes that the impurity atom of mass m is attached to the host atom of mass M_{nn} (nn stands for nearest neighbor) by a spring of constant k results in the following relation between the LVM frequency and the mass of both the impurity and the neighboring atoms ([24],[25]):

$$\omega_L^2 = k(\frac{1}{m} + \frac{1}{\chi M_{nn}}) \tag{2.18}$$

where χ is an empirical parameter related to the local bond bending and stretching force constants. According to theoretical models such as the cluster method, the second neighbor motion does not have a significant effect on the vibrations of the impurity atom, and equation 2.18 provides a good approximation for the LVM frequency in most cases [24]. According to theoretical calculations, the value of the parameter χ can vary only in the range of 1.3 to 6.4 [26] and its typical value is 2. This criterion can be used to determine the lattice sites of the impurities, however; it is not always successful. For example it was used to rule out the presence of substitutional carbon donors in InP [27] but it predicts a wrong lattice site of carbon in AlAs (χ=5.9 for C_{As} and χ=2.1 for C_{Al}).

The LVMs of impurities can be detected both by IR spectroscopy and Raman spectroscopy. Since the selection rules for these methods are usually different, they can be used together to determine all the LVMs of the impurities and their related complexes.

2.4.2 Fourier transform IR spectroscopy(FTIR)

FTIR spectroscopy has been proven to be the preferred method of IR spectroscopy, due to the higher optical throughput in this method compared to dispersive methods.

The main part of a FTIR spectrometer is the Michelson interferometer. It includes a beamsplitter that divides the source light into reflected and transmitted beams. Two beams are reflected back to the beamsplitter by a movable and a fixed mirror and are

then focused on the sample. Figure 2.11 shows a simple diagram of a typical FTIR spectrometer.

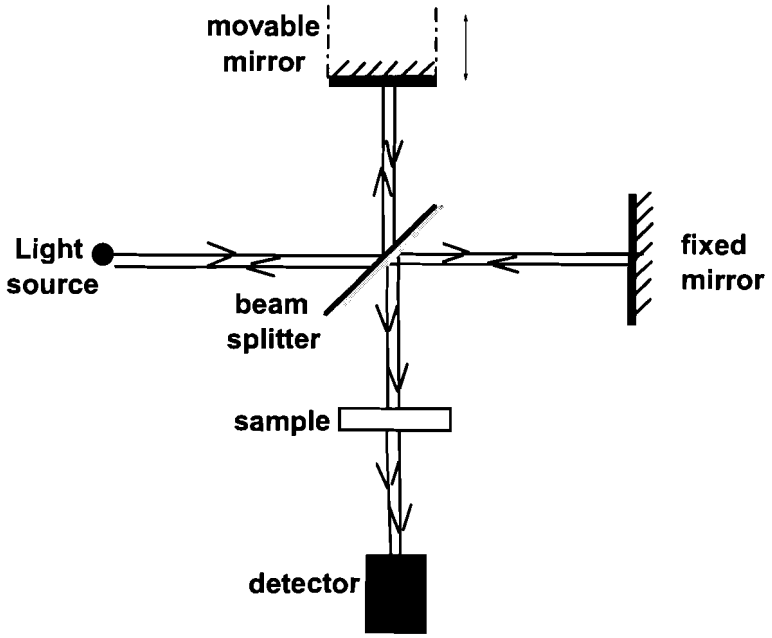

Figure 2.11: A simple diagram of a FTIR spectrometer.

Since the position of the movable mirror changes constantly, the beams recombine with each other with a phase difference and the signal measured by the detector is the result of their interference. The graph of this signal versus the path difference is called an interferogram and is basically the sum of the interference patterns for all the frequencies of the light source. Therefore by the FTIR method the response of the sample to all the frequencies of the light source can be measured simultaneously. A typical interferogram is shown in figure 2.12. The maximum at zero corresponds to equal distances of the mirrors from the beamsplitter that results in constructive interference for all the frequencies and therefore the peak is called the white light position. The Fourier transform of the interferogram gives the final IR spectrum in

the frequency range.

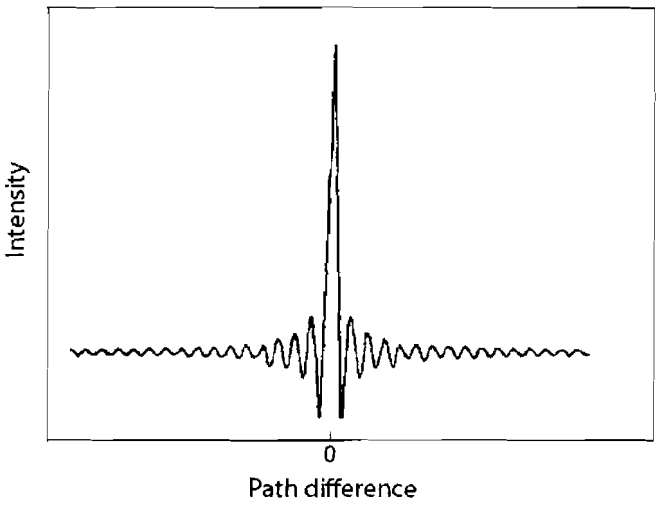

Figure 2.12: A typical interferogram obtained by an FTIR spectrometer.

IR absorption measurements of this work were performed by professor Thewalt's group at Simon Fraser University. A Bomem DA8 interferometer was used with a Mylar beamsplitter and a Si:B detector at 4.2 K for the low energy modes and a CaF_2 beamsplitter and InSb detector at 77 K for the higher energy modes. For both sets of measurements the samples were cooled by flowing He gas in a Varitemp Dewar, with polypropylene windows for the low-energy measurements and ZnSe windows for the high-energy region.

2.5 Raman spectroscopy

Raman spectroscopy is one of the main characterization methods used in this work. Due to the high sensitivity for thin layers and the nondestructive nature of the technique, Raman spectroscopy has been widely used to study the lattice dynamics as

well as the electronic properties of the semiconductor layers. Also, together with infrared spectroscopy, it has been very useful for the investigation of impurities in semiconductor materials by providing information about their vibrational properties. In this section, we discuss the theory of the Raman spectroscopy, different light scattering mechanisms, and the selection rules. A brief description of the experimental instrumentation will follow.

2.5.1 Theory of Raman spectroscopy

Raman spectroscopy is based on inelastic light scattering by elementary excitations of the lattice such as phonons, plasmons, and coupled phonon-plasmons. An incident photon with energy $\hbar\omega_i$ interacts with the lattice excitations and as a result, a scattered photon with energy $\hbar\omega_s$ is produced. The frequencies of the elementary excitations are determined by the Raman experiment using the energy conservation law:

$$\hbar\omega_s = \hbar\omega_i \pm \hbar\omega_q \tag{2.19}$$

where $\hbar\omega_q$ is the energy of the elementary lattice excitations. The - sign refers to the so called Stokes processes in which an elementary excitation is generated. The + sign corresponds to the anti-Stokes processes which result in the annihilation of a lattice phonon or local mode.

The wavevector of a lattice excitation can be calculated using the conservation of crystal momentum law:

$$k_s = k_i \pm q \tag{2.20}$$

where k_s and k_i are wavevectors of the scattered and incident photons, respectively. In a first order process where only a single elementary excitation is involved in the scattering, $\hbar\omega_q$ and q are the energy and the wavevector of that specific mode, respectively, but for higher order excitations, the values are the sum of the corresponding values for all of the involved excitations.

The magnitude of the wavevector of the scattered light is dependent on the experimental geometry. Figure 2.13 shows different geometries that are usually used in Raman spectroscopy. The magnitude of this wavevector is maximum for the backscat-

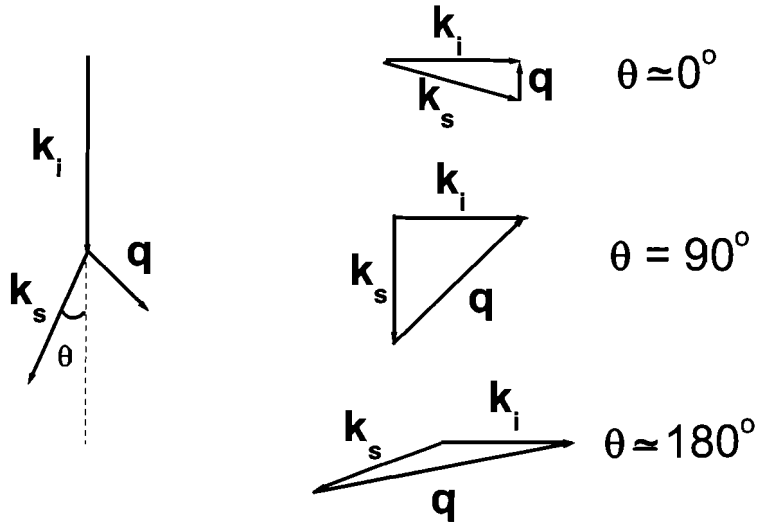

Figure 2.13: Diagrams of different Raman scattering geometries.

tering geometry when $\theta \simeq 180$ °. In the visible and near infrared region q is in the range of $0 \leq q \leq 10^6$ cm^{-1} which is two orders of magnitude smaller than the wavevectors corresponding to the Brillouin zone boundaries. Therefore the first order excitations are at or near the Brillouin zone center.

Light scattering susceptibilities The scattered light of the Raman process can be described as the radiation of an oscillating electric dipole resulting from the simultaneous action of the incident light and the elementary excitations. The induced polarization that oscillates at the frequency ω_s, can be described using a generalized dielectric susceptibility tensor [28]:

$$P(\omega_s) = \epsilon_0 \tilde{\chi}(\omega_i, \omega_s) E(\omega_i) \tag{2.21}$$

where $P(\omega_s)$ is the oscillating polarization , $\tilde{\chi}(\omega_i, \omega_s)$ is the susceptibility tensor, and $E(\omega_i)$ is the electric field of the incident light. The Raman scattering intensity can be

calculated using the dipole radiation intensity:

$$I_s \propto |e_s \tilde{\chi}(\omega_i, \omega_s) e_i|^2 \tag{2.22}$$

where e_i and e_s are the polarization unit vectors of the incident and scattered light, respectively.

The components of the electric susceptibility tensor can be Taylor-expanded in terms of Q_js, the amplitude of the phonon modes of frequency ω and wavevector q, to show the effect of the lattice phonons on the electric susceptibility:

$$\chi_{\alpha,\beta}(\omega_i, \omega_s) = \chi^0_{\alpha,\beta}(\omega_i) + \sum Q_j \left(\frac{\partial \chi_{\alpha,\beta}(\omega_i)}{\partial Q_j}\right) + \sum Q_j Q_{j'} \frac{1}{2} \left(\frac{\partial^2 \chi_{\alpha,\beta}(\omega_i)}{\partial Q_j \partial Q_{j'}}\right) + \ldots \tag{2.23}$$

where ${\chi_{\alpha,\beta}}^0(\omega_i)$ is the electric susceptibility without the phonons effect, and α and β are the directions of the scattered and the incident electric fields. The above expansion only includes the symmetry allowed terms. The derivatives in the above equation are the tensor components of the Raman polarisability ($\tilde{\chi}$) or the so-called Raman tensor ($\tilde{R}$). The first and second terms in equation 2.23 refer to the first and second order scattering processes, respectively.

Raman light scattering processes can be described by using three electronic transitions:

- the excitation of an electron from the ground state to a real or virtual excited state: the creation of an electron-hole pair due to the annihilation of the incident photon.
- the interaction of the electron-hole pair with the lattice through the creation or annihilation of phonons or local vibrations of impurities (LVMs).
- the creation of the scattered photon by recombination of the electron-hole pair.

Figure 2.14 shows a schematic diagram of these processes.

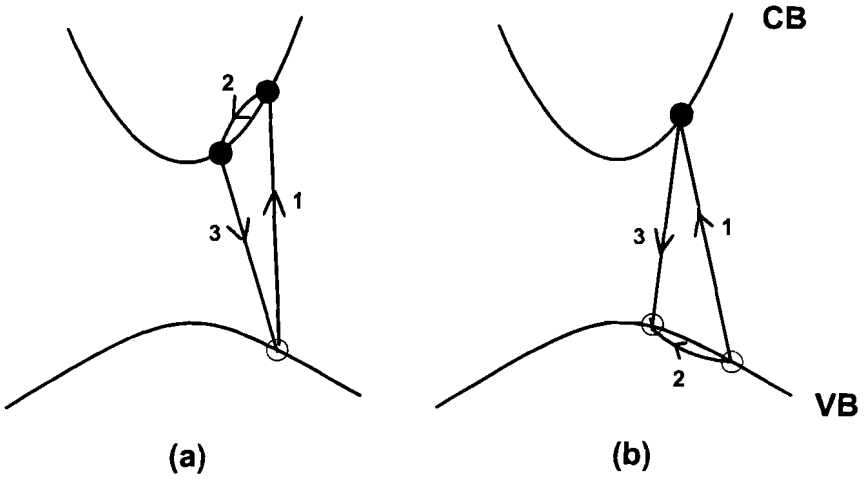

Figure 2.14: Schematic diagrams of resonance Raman scattering processes. (a) the created electron is scattered by an excitation, (b) the created hole is scattered by an excitation. CB and VB refer to conduction and valence bands, respectively.

Selection rules An elementary excitation mode is called Raman-active if the first term in the right hand side of equation 2.23 is nonzero. The Raman activity is determined by the symmetry properties of the lattice and that specific mode. For a Raman active mode, the selection rules determine the polarization directions of the incident and scattered light that lead to a nonzero scattering intensity (equation 2.22).

There are some methods to determine the number and the symmetry of the Raman-allowed modes for a material. Discussion of these methods is out of the scope of this work and can be found in many references [29, 30].

According to group theory arguments, for materials with a center of inversion such as Si crystal, the irreducible representations of the phonons have either even or odd symmetry. Since the Raman tensor is of even symmetry, the odd symmetry modes can not be observed with Raman spectroscopy. The reason that only even symmetry

modes can be Raman active is that the coupling between the incident light electric field and the lattice modes is not direct in resonant Raman scattering and is mediated by interband excitations (Figure 2.14). Only even-symmetry phonons can couple two electronic states with the same symmetry. On the other hand, in IR spectroscopy, modes couple directly to the incident light. Since the dipole moment of the mode is a vector and changes sign under inversion, only odd modes can be IR-active. Therefore for these kinds of materials, elementary modes can be either Raman- or IR-active and these two methods are complementary to each other. For materials lacking a center of inversion such as III-V semiconductors, lattice modes can be observed in both Raman and IR spectroscopy.

Resonant Raman scattering There are two parameters that are important in determining the Raman scattering cross section: one is the probability of interband electronic transitions, and the other is the strength of the electron-phonon interactions. The closeness of the incident light frequency to the fundamental or higher energy gaps of the material band structure results in an enhancement in the scattering cross section by increasing the probability of the interband transitions. This can be understood if we use third-order quantum perturbation theory to calculate the susceptibility when an electron gets exited from the ground state to state $|e\rangle$ and scattered to state $|\acute{e}\rangle$ by electron-phonon interactions [28]:

$$\chi_{\alpha,\beta}(\omega_i,\omega_s) = \frac{e^2}{m_0^2.\omega_s^2.V}\sum \frac{\langle 0|p_\alpha|\acute{e}\rangle\langle\acute{e}|H_{E-L}|e\rangle\langle e|p_\beta|0\rangle}{(E_{\acute{e}}-\hbar\omega_s)(E_e-\hbar\omega_i)} \tag{2.24}$$

where m_0 is the mass of electron, V is the scattering volume, p_α and p_β are the dipole operators of the incident and scattered light, and H_{E-L} is the electron-phonon interaction Hamiltonian. Raman scattering processes that involve light frequencies close to the gap energies are called resonance Raman scattering.

Enhancement of the scattering cross section in resonance Raman scattering makes the observation of weak features possible. Also it can be used to investigate the electronic band structure by varying the energy of the incident light and studying the scattering cross section.

2.5.2 Raman scattering instrument

Raman scattering measurements in this work were performed by myself in Dr. Chen's laboratory at Simon Fraser University. Figure 2.15 shows the Raman spectroscopy setup with a triple monochromator. The main components of the setup are: a monochromatic light source, a spectrometer, and a sensitive detector.

Light source The intensity of the scattered light in the Raman scattering process is very weak compared with IR spectroscopy. Therefore; lasers are the appropriate light sources for this kind of spectroscopy because they provide an intense source of monochromatic light. Kr^+ and Ar^+ lasers are usually used in the spectral regions of green to ultraviolet and infrared to ultraviolet, respectively. The strongest lines for the Kr^+ laser are 647 and 676 nm and for the Ar^+ laser are 514, 488, and 457 nm. We used the 488 and 514 nm lines of an Ar^+ laser for measuring InAs and GaSb samples, respectively.

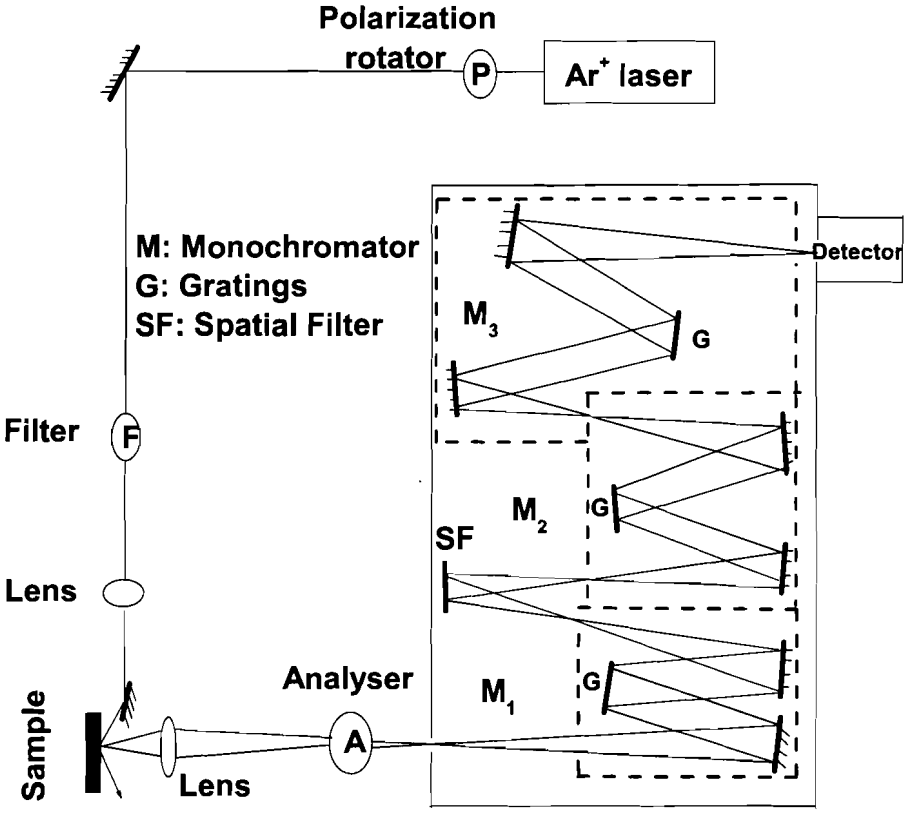

Figure 2.15: A schematic view of a triple spectrometer for Raman spectroscopy.

The closeness of the 488 nm (2.54 eV) laser line to the E_1 gap energy of InAs (2.61 eV) resulted in the resonant Raman scattering process. Filters are usually used to eliminate the unwanted nonlasing emission lines from the incident light. A polarization rotator and an analyzer can be put in front of the laser and before the spectrometer slit, respectively, to vary the polarization of the incident light and measure the polarization of the scattered light.

Raman spectrometer The scattered light enters the spectrometer through a narrow slit after being focused by a lens. The spectrometer consists of a grating monochromator for the frequency analysis of the scattered light. The grating separates the scattered light into the component wavelengths and monochromator transmits the Raman lines to the detector. The spectrometer used in this work had a triple monochromator which provides a very high contrast to separate the very weak Raman light from the much stronger nearby elastically scattered light (figure 2.15). In this kind of setup, light hits a subtractive double monochromator first (M_1 and M_2) which filters out the elastically scattered light, and then it hits the third monochromator (M_3) to lead the inelastically scattered Raman light to the detector .

Detector Different kinds of detectors such as diode arrays, charge coupled devices (CCD), and position sensitive detectors have been used for detecting the scattered light in Raman spectroscopy. For the Raman setup used in this work, a CCD cooled with liquid nitrogen was used. This kind of detector provides a high signal to noise ratio and enables data to be gathered for long periods of time.

2.5.3 Applications of Raman spectroscopy in semiconductor characterization

Raman spectroscopy has been widely used to study the crystal lattice and electronic parameters of semiconductors. It can provide information about strain, orientation, and composition of the crystal lattice as well as electronic properties such as impurities, carrier concentration, and energy band structure.

Structural properties The presence of stress in semiconductor heterostructures affects the lattice vibrations by inducing lattice deformation. Therefore determining the exact frequencies of the phonons detected in Raman spectroscopy can be used to calculate the amount of strain in heterostructures [31, 28]. Crystal orientation is another lattice parameter that can be determined by Raman spectroscopy. According to selection rules, Raman activity of the longitudinal optical (LO) and transverse optical (TO) modes of zincblende structures depends on the orientation of the surface of the crystal.

Although much of this information about the lattice properties can be obtained by other methods such as X-ray diffraction, the advantage of the Raman spectroscopy is the lower required thickness for the measurement. Also, Raman spectroscopy provides the possibility of doing a depth profile by changing the wavelength of the incident light that changes the penetration depth of the light.

Electronic properties In this work Raman spectroscopy was mostly used to study the properties of impurities in semiconductors. Impurities change the Raman spectra of semiconductors not only by introducing local vibrational modes, but also by interacting with the lattice through the carriers. For the impurity atoms that are lighter than the host atoms, the vibrational modes associated with the motion of these atoms are localized and do not couple with the phonon modes. A simple explanation for this is that heavier host atoms can not follow the fast motion of these light impurity atoms. Although the LVMs of impurities are usually very weak (due to low concentration of impurities compared to host atoms), they can be detected by Raman spectroscopy even in moderate concentration. For example, carbon impurities of concentration 10^{17} cm^{-3} in silicon can be detected by Raman spectroscopy [32]. The intensity of LVMs can be used to calculate the impurity concentration in materials; however, the existence of a previous calibration is necessary.

Impurities can also interact with the lattice of polar semiconductors via coupling of the optical phonons with the macroscopic electric field of plasmons. This coupling happens when the frequency of the plasmons is close to optical phonon frequencies.

In that case the lattice phonon and the plasmon modes are replaced by two Raman-active coupled Plasmon-LO-Phonon modes (PLP): one at low frequency (ω^-) and one at higher frequency (ω^+). The frequencies of these modes can be calculated from the dielectric function ($\epsilon(\omega,q)$), considering that for the longitudinal modes this function should be zero [28]:

$$\epsilon(\omega,q) = \epsilon_\infty + \frac{\omega_{TO}^2.(\epsilon_s - \epsilon_\infty)}{\omega_{TO}^2 - \omega^2 - i\omega\Gamma} - \frac{\omega_p^2}{\omega^2 - \frac{3}{5}.v_F^2.q^2} \tag{2.25}$$

where Γ is the phonon damping constant, and v_F is the Fermi velocity. ω_p is the plasma frequency that can be calculated by the following equation:

$$\omega_p^2 = \frac{4\pi n e^2}{m^* \epsilon_\infty} \tag{2.26}$$

where n is the carrier concentration, m^* is the carrier effective mass, and ϵ_∞ is the high frequency dielectric constant. Using typical values for the parameters in the above equation it can be shown that PLP modes appear for carrier concentrations in the range of 10^{17} to 10^{19} cm^{-3} . Considering the sensitivity of the PLP mode frequencies to n, these features can be used to determine the carrier concentrations.

Chapter 3

Growth and characterization of InAs:C

Carbon has been of interest as a p-type dopant for most III-V semiconductors such as GaAs, GaSb, and AlAs. Local vibrational mode studies have shown that it occupies the group V lattice site in these materials and becomes an acceptor [1, 2, 3]. Due to the high solubility and low diffusivity of carbon, doping levels as high as 5×10^{20}cm^{-3} can be easily achieved for these materials [4]. InP and InAs are the only III-V semiconductors that show different characteristics after being doped with carbon. InP becomes n-type or semi-insulating (depending on the growth conditions) and InAs shows n-type conductivity after being doped with carbon. Although a lot of research has been done about p-type carbon doping of III-V semiconductors, the properties of carbon in these two In-containing materials, especially InAs, have not been investigated in detail.

There are several reports of the intentional carbon doping of InP using different methods. Pearton *et al.* reported donor concentrations as high as 3×10^{19} cm^{-3} with co-implantation of carbon and phosphorous into InP and they assumed that carbon occupies the In lattice site and incorporates as a donor [33]. OMVPE growth of InP at the substrate temperatures between 440 and 500°C using TMIn as the source of carbon was reported by Stockman [34]. They achieved n-type doping levels as high as 1.3×10^{18} cm^{-3} which they attributed to the presence of carbon, although no physical

model was provided. According to their results, the ratio of the electron concentration to the carbon concentration (n/[C]) was ~5%-15%. This was interpreted as evidence of compensation by shallow or deep acceptors. They also observed that the current gain in InP/InGaAs HBTs was reduced by using intentionally carbon-doped InP, which could be the result of the presence of some deep levels in InP. The behavior of carbon in InP has been studied by Theys *et al.* by introducing atomic hydrogen in chemical beam epitaxial (CBE)-grown InP doped with CBr_4 [35]. Their secondary ion mass spectroscopy (SIMS) measurements showed a strong interaction between carbon impurities and hydrogen atoms. This was different from the behavior of other n-type dopants such as silicon. Also the electron concentration of their samples increased by introducing atomic hydrogen. Based on these facts and also the low n/[C] ratio for InP:C, they suspected the presence of negatively charged carbon acceptors that leads to highly compensated material. Also the hydrogen passivation of these acceptors explains the increase of the electron concentration observed after introducing atomic hydrogen.

Ramsteiner *et al.* grew carbon doped InP by the MOMBE technique [36]. Their samples showed n-type conductivity with electron concentrations as high as 6×10^{18} cm^{-3} . They observed a peak at 220 cm^{-1} in the Raman spectra of their samples which they attributed to the gap mode of C_{In} lattice sites. The assignment of this line to carbon donors was not conclusive because there was no correlation between the intensity of this line and the carbon concentration measured by SIMS. On the other hand, Newman *et al.* observed a line at 546.9 cm^{-1} in the IR spectra of semi-insulating carbon-doped InP samples grown by OMVPE [37]. They assigned this line to carbon acceptors occupying P lattice sites based on the amount of isotopic shift of the line. They also detected different modes of the C-H complexes with hydrogen atoms occupying the bond centered positions. Raman spectroscopy of the semi-insulating InP:C samples grown by OMVPE, revealed some LVMs in the frequency region around 1800 cm^{-1} [38]. These lines were attributed to split-interstitial dicarbon complexes in comparison with similar LVMs detected for highly doped GaAs:C samples annealed at temperatures higher than 600 °C [39]. According to the theoretical calculations for GaAs:C, this defect is a deep donor with an energy level near the midgap of GaAs [40].

The presence of these defects provided an explanation for the semi-insulating conductivity of the carbon-doped samples, where carbon acceptors were highly compensated by these donor species.

To the author's knowledge, there are only a few reports of the intentional carbon doping of InAs and those were done by molecular beam epitaxy (MBE) [7, 8], metal organic molecular beam epitaxy [9], and OMVPE [41] methods. According to Schoenfeld *et al.* [7], MBE-grown samples showed n-type conductivity except for a very narrow window of growth conditions which resulted in p-type samples with very low hole concentrations. No explanation of this behavior was provided. Ito *et al.* [8] also reported n-type conductivity and assumed that carbon atoms occupy the In lattice sites in this material and become donors. The report of OMVPE-growth of carbon-doped InAs [41] is mostly focused on the kinetics of carbon tetrachloride decomposition during the growth without any discussion of the properties of the layers.

In this chapter, the OMVPE growth of carbon-doped InAs layers will be discussed briefly. After that the effect of carbon doping on the lattice properties of InAs investigated by HRXRD measurements will be introduced. The results of Raman and IR spectroscopy measurements of samples together with a discussion of the lattice site of carbon in InAs will be followed.

3.1 OMVPE growth of carbon-doped InAs

InAs epilayers were grown on (100) oriented GaAs and InAs substrates in a vertical OMVPE reactor at a pressure of 50 Torr and substrate temperatures of 500, 400, 375, and 355 °C. TMIn, TBAs , natural CBr_4, and CCl_4 with a mixture of 70% ^{13}C and 30% ^{12}C were used as the precursors with the V:III ratios of 12 and 6.

3.1.1 Effects of the substrate temperature on the doping level

The substrate temperature has been shown to be an important factor in the incorporation of carbon during the OMVPE growth of III-Vs. Buchan *et al.* observed the reduction of carbon incorporation from the CCl_4 source into GaAs by increasing the

substrate temperature [42]. They explained this by the higher desorption rate of the CCl_4 molecules from the surface at high temperatures. Gardner *et al.* have reported a similar effect for carbon-doped InP samples [43]. According to their SIMS data, the concentration of carbon decreases by increasing the growth temperature in the range of 400-500°C and this was accompanied by an increase in the resistivity of the samples.

In order to investigate the effects of the substrate temperature on the incorporation efficiency of carbon in InAs, secondary ion mass spectroscopy (SIMS) measurement was performed by Charles Evans and Associates on a sample composed of four layers of InAs grown at different temperatures and with the same CBr_4 flow rate. The results are shown in figure 3.1.

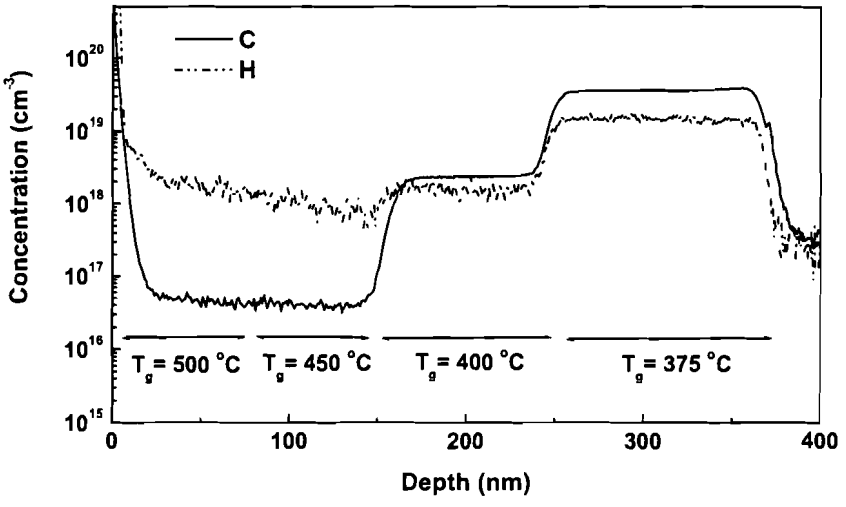

Figure 3.1: The results of SIMS measurement of a sample composed of 4 layers grown at temperatures of 500, 450, 400, and 375°C using a constant [CBr_4] flow.

Although the concentration values are not exact due to the lack of calibration standards for carbon in InAs, they can still be used to make a comparison among the layers. These results clearly show the strong dependence of the carbon incorporation

on the growth temperature. There is no measurable difference between the carbon concentration of the layers grown at 500 and 450°C. This is likely due to background limitations for detection of carbon by SIMS. Lowering the temperature to 400 and 375°C significantly increased the amount of carbon incorporation. The other interesting result from this measurement was that hydrogen was also present in all of the layers and its concentration increased with decreasing growth temperature.

Although InAs:C samples grown by MBE at 450°C showed electron concentrations as high as 5×10^{19} cm^{-3} [7], the electron concentration of our samples measured by the Hall method did not increase beyond $6\times$ 10^{18} cm^{-3} for the samples grown at 375°C. The doping efficiency decreases by increasing the growth temperatures. Figure 3.2 demonstrates the electron concentrations of the samples grown at four different temperatures of 500, 400, 375, and 355°C. As seen in the figure, there are two regions

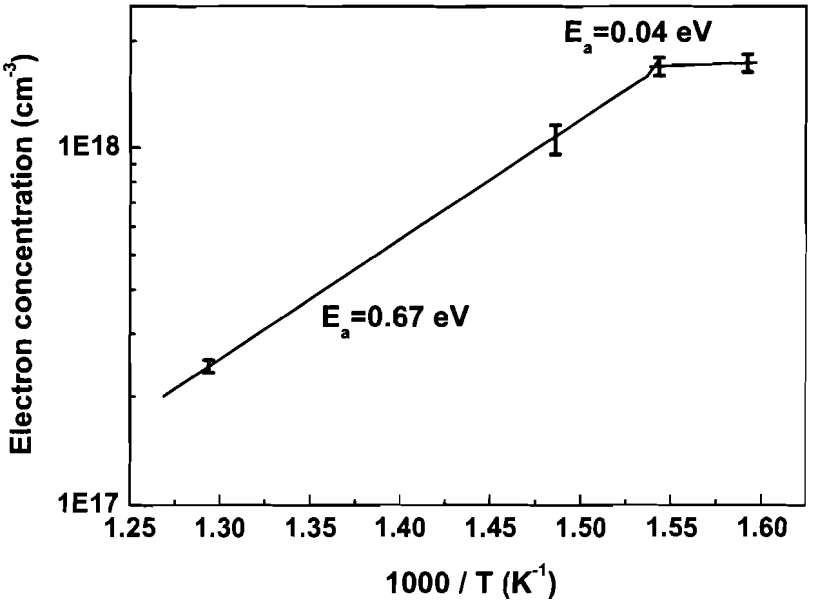

Figure 3.2: The electron concentration of samples grown at different temperatures with the same CBr_4 flow rate.

with different activation energies. The electron concentration changes by almost an order of magnitude in the temperature range of 400-500 °C with an activation energy of 0.67 eV, however, there was little change between 355-375 °C. Based on these two temperature points, an activation energy of 0.04 eV can be estimated. Similar behavior has been reported for metal organic molecular beam epitaxy (MOMBE) grown carbon-doped InP by Oh *et al.* [44]. For growth temperatures higher than 350°C, the activation energy was 1.99 eV, almost three times higher than that in InAs. Their explanation for the dependence of the electron concentration on the growth temperature was based on the assumption that the n-type conductivity is due to carbon donors originating from the tertiarybutylphosphine (TBP) source so that the electron concentration could be controlled by varying the substrate temperature. We'll explain this after introducing the source of electrons in InAs:C (section 3.3.4).

The dependence of electron concentration on the CBr_4 flow rate was studied at two temperatures of 400 and 375 °C and the results are demonstrated in figure 3.3. At 400 °C, carrier concentration increased linearly with CBr_4 flow rate; however, the rate of increase was very low. Lowering the substrate temperature to 375 °C, caused a significant increase in the concentration of electrons and the rate of the change as well. Increasing [CBr_4] beyond 1.5 μmol/min did not make a significant change in the electron concentration and it resulted in a degradation of the surface morphology.

In summary the correlation between [CBr_4] and the electron concentration in our data shows that carbon-related donors are present in doped material.

3.1.2 Effect of substrate temperature and [CBr_4] on the growth rate

The growth rate of the InAs samples was highly affected by the substrate temperature and the CBr_4 flow rate. Figure 3.4 shows the change of the growth rate with carbon concentration at two substrate temperatures of 400 and 375 °C. The reduction of the growth rate by [CBr_4] is the result of surface etching caused by bromine. Etching of III-V semiconductor layers such as GaAs by the chlorine and bromine released from the decomposition of CCl_4 and CBr_4 has been observed during OMVPE growth

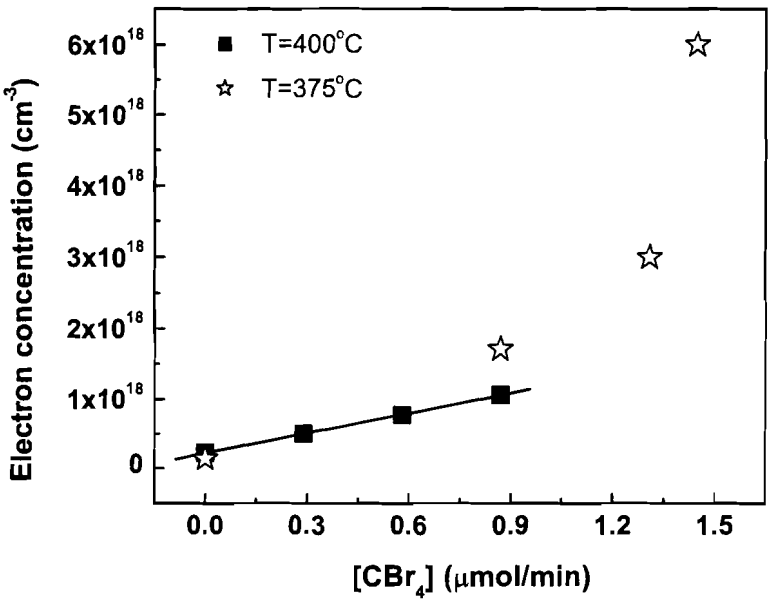

Figure 3.3: The electron concentration of InAs:C samples grown at 400 and 375 °C with different CBr_4 flow rate.

[45, 46]. These elements react with the group III atoms and result in the etching of the surface layer. The pyrolysis reaction of CBr_4 is as follow [46]:

$$CBr_4 + 2H_2 \leftrightarrow C + 4HBr$$

The released HBr reacts with In atoms according to the following equation:

$$In + 3HBr \leftrightarrow InBr_3 + \frac{3}{2}H_2$$

Our data show that the InAs growth rate at both temperatures is inversely proportional to [CBr_4]; however, the rate of change is higher at lower temperature.

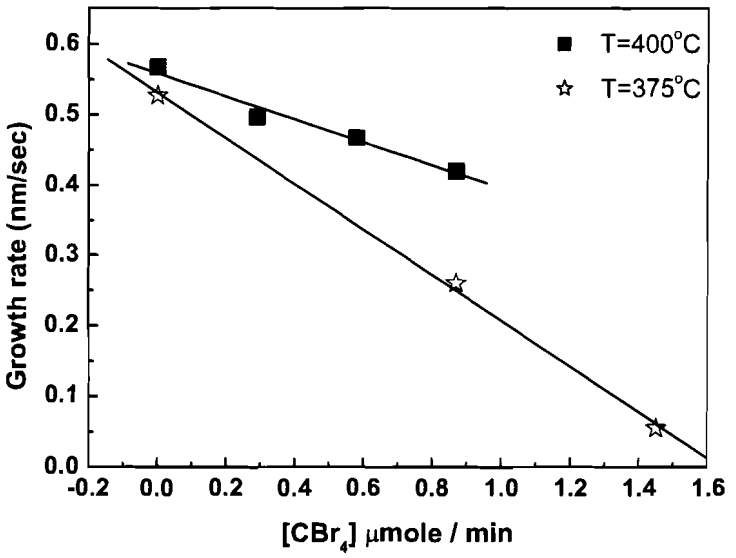

Figure 3.4: Growth rate of InAs:C grown at 400 and 375 °C with different CBr_4 flow rates.

3.2 Structural properties of InAs:C

Considering the small covalent radius of carbon (0.77 Å) compared to that of In (1.67 Å) and As (1.20 Å), introducing carbon into InAs decreases the lattice constant, regardless of the lattice site that it occupies. Therefore there will be a lattice mismatch between the doped epilayer and the undoped substrate that can be estimated by some simple assumptions.

We consider the case that carbon atoms occupy the As lattice sites. The In-C bond length can be simply calculated by adding the covalent radii of both atoms (0.77 + 1.67 = 2.44 Å). Although InC is not a real crystal, its lattice constant in an imaginary zinc-blende crystal can be estimated as follows:

$$a_{InC} = \frac{4}{\sqrt{3}}(r_{In} + r_C) = 5.635\mathring{A} \tag{3.1}$$

Similar arguments were found to predict the lattice shrinkage due to carbon doping of

GaAs [47] and GaSb [11]. The lattice constant of carbon-doped InAs can be calculated using Vegard's law:

$$a_{InAs_{1-x}C_x} = x a_{InC} + (1-x) a_{InAs} \tag{3.2}$$

where x is the fraction of InC. XRD patterns together with dynamical XRD simulations were used to estimate the thickness of the layers and the composition of InC (x). The perpendicular strain of the epilayer can be calculated using the following relationship[16]:

$$\triangle a_{\perp}/a = -\cot\theta_B \triangle\theta \tag{3.3}$$

where θ_B is the Bragg angle of the undoped InAs and $\Delta\theta$ is the angular separation between the undoped and doped InAs calculated from the rocking curves. The lattice constant of relaxed InAsC can be calculated using the following equation:

$$a_{InAsC}(relaxed) = \frac{2\nu}{1+\nu} a_{\parallel} + \frac{1-\nu}{1+\nu} a_{\perp} \tag{3.4}$$

where ν is the poisson ratio of InAs (0.352) and $a_{\parallel}$ is the lattice constant parallel to the interface which for the coherently strained layer is equal to the lattice constant of InAs (6.0583 Å). Figure 3.5 demonstrates the XRD patterns together with the relative lattice contraction values ($\Delta a_{\perp}/a=(a_{\perp}-a_{\parallel})/a_{\parallel}$) for the samples grown at 375°C and doped with different CBr_4 pressures. As seen in the figure, the lattice mismatch between the substrate and the carbon-doped layer increases by increasing the CBr_4 flow rate to 1.02 μmole/min and it does not change by increasing [CBr_4] beyond this value. Assuming that isolated substitutional carbon atoms are the main cause of the lattice mismatch, we can conclude that at higher CBr_4 flow rates, either carbon does not incorporate in InAs layers in the form of substitutional defects or carbon atoms become aggregated.

Substitutional defects are not the only form of carbon incorporation in the layers. It is known for other III-V semiconductors such as GaAs and InP that other kinds of defects such as carbon-hydrogen complexes, interstitial carbon atoms, and dicarbon defects are also present in the samples. All these defects affect the lattice of InAs in some way; however, the substitutional defects have the biggest effect (this will be discussed in more detail in the next chapter).

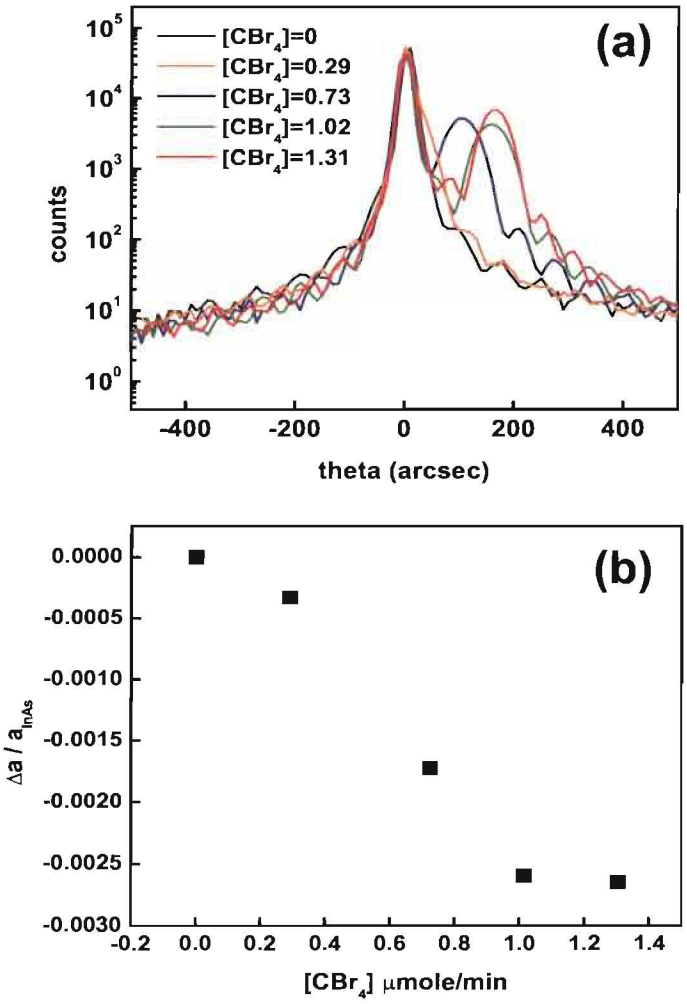

Figure 3.5: (a) XRD patterns and (b) relative lattice contraction for InAs:C samples grown at 375 °C and doped with different CBr_4 flow rates.

Table 3.1: A summary of XRD measurement results for InAs:C samples grown at 375°C.

Sample	$[CBr_4]$ (μmole/min)	$\Delta a_\perp/a$	x_{InC}	$[C_{As}]$ (cm^{-3})
4950	0	0	0	0
4953	0.29	-0.00033	0.23×10^{-2}	1.73×10^{19}
4951	0.73	-0.00173	1.18×10^{-2}	9.06×10^{19}
4952	1.02	-0.00260	1.78×10^{-2}	1.36×10^{20}
4954	1.31	-0.00265	1.81×10^{-2}	1.39×10^{20}

If we neglect the effect of the other kinds of defects on the lattice constant, it is possible to make an assumption about the concentration of carbon on the As lattice sites in the layers by using the values of InC composition (x) using the following relationship:

$$a_{InAsC(relaxed)} - a_{InAs} = \frac{4}{\sqrt{3}}(r_C - r_{As})\frac{[C_{As}]}{N_o} \tag{3.5}$$

where N_o=1.795×10^{22} cm^{-3} is the concentration of As atoms. Table 3.1 summarizes the calculated values for the relative lattice contractions and the concentration of carbon atoms on the As lattice sites.

The concentrations of carbon atoms calculated from the XRD data are an order of magnitude higher than the electron concentrations measured by the Hall method at room temperature. There are two possible explanations for this contrast: one is that the role of the substitutional carbon atoms on the lattice contraction of InAs:C might be overestimated in the above calculations and other defects may also have significant effects on the lattice contraction. The second explanation is that carbon acceptors occupying the As lattice sites (as assumed in the above calculations) are compensated by carbon-related donors.

3.3 Local vibrational mode study of carbon-doped InAs

As mentioned before, studying local vibrational modes of impurities in semiconductors provides useful information such as the lattice site and concentration of the impurities. In this work, we have used Raman and FTIR spectroscopy methods to study the vibrational properties of carbon-doped InAs samples.

3.3.1 Raman scattering by isolated carbon defects

In this section, we report on Raman spectroscopy results for the carbon-doped InAs samples. We used a triple spectrometer in a quasi-backscattering geometry for these measurements. The 488 nm line of an Ar-ion laser with a power of 60 mW was focused on a 50 $\times$ 500 μm^2 area. The energy of this laser line (2.54 eV) is very close to the E_1 gap energy of InAs (2.61 eV) and as a result, resonant Raman scattering occurs. The penetration depth of this laser line in InAs is $1/\alpha(\omega)= 1/(5\times10^5\ cm^{-1}\ )$ =20 nm, where $\alpha(\omega)$ is the absorption coefficient.

Fig 3.6 demonstrates a typical Raman spectrum for InAs:C samples in the wavenumber range of 130 to 600 cm^{-1} . There are two main features in this spectrum: one at 237 cm^{-1} and the other at 477 cm^{-1} . The first peak is the longitudinal optical (LO) phonon mode of InAs [48] and the second one is the 2LO mode which is likely strong due to the resonant Raman scattering [49]. The slight shoulder that appears on the left side of the LO peak can be related to couple plasmon-LO phonon modes [50]. In addition to these peaks, two other relatively weak lines exist at 527 and 386 cm^{-1} .

In order to examine any possible relationship between these new features and carbon doping, samples with different carbon doping levels were measured by Raman spectroscopy. Figure 3.7 shows the results of these measurements. The 2LO peak was used to normalize the spectra in order to eliminate the errors caused by variations in the laser power and the optical geometry.

As seen in the figure, the lines at 527 and 386 cm^{-1} appear only on the spectra of the doped samples and their intensity is correlated by the amount of CBr_4. This

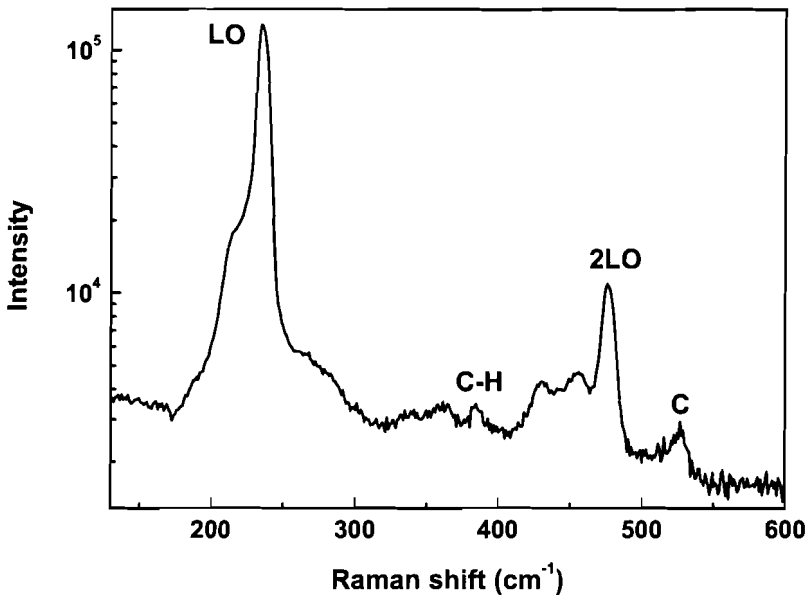

Figure 3.6: Room temperature Raman spectrum of an InAs:C sample grown at 375°C.

clearly shows that both lines are related to carbon impurities. The frequency of the line at 527 cm^{-1} is very close to the LVM frequency of the substitutional carbon acceptors in other III-V semiconductors. To verify the assignment of this line to an isolated substitutional impurity, we performed Raman measurements on two sets of samples: the first one doped with natural C (~99% ^{12}C) and the second one doped with a mixture of ^{12}C and ^{13}C. Figure 3.8 shows the results.

In the spectrum of the sample doped with both isotopes, another peak appears at the wavenumber of 508 cm^{-1} . The isotopic frequency shift of $\omega_{13}/\omega_{12} = 1.037$ is very close to $\sqrt{13/12}$=1.04 (see equation 2.18 for the case where M $\gg$ m). This confirms the assignment of the line at 527 cm^{-1} to an isolated substitutional carbon impurity. Using equation 2.18 was not helpful in determining the lattice site of the carbon, because replacing M_{nn} with the masses of In and As gives two values of 2.31 and 1.51, respectively, for χ that both lie in the acceptable range for this parameter.

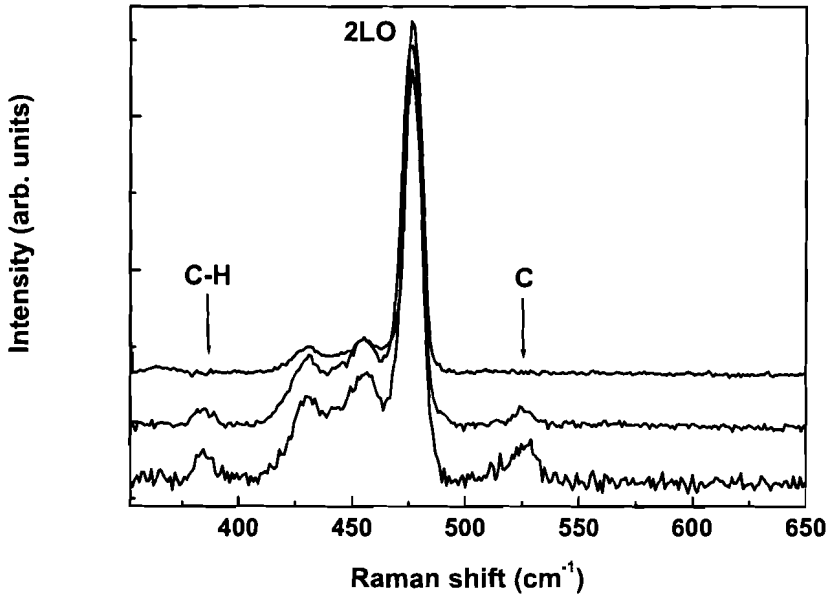

Figure 3.7: Room temperature Raman spectra of samples grown at 375 °C, from top to bottom: undoped, $[CBr_4]$=0.87, and 1.45 $\mu mole/min$.

Figure 3.9 is a plot of the carbon LVM energies in wavenumbers for different III-V semiconductors as a function of the lattice constants. The fitted line through the InP and InAs data points has a slope that is very close to the average slope of the other carbon acceptor data. As seen in the graph, there are three different classes of semiconductors with the same group III atom for each one. The reduction of the LVM energy by the radius of the group III atom can be explained with the strength of the C_V-III bond. As mentioned at the beginning of this chapter, it is known for all III-V semiconductors except InAs, that carbon occupies the group V lattice sites in these materials and becomes an acceptor. Therefore the energy of the carbon LVM depends on the strength of the C-III bond. The C-III bond length for different III-V materials together with the bond strengths of metal-CH_3 are summarized in table 3.2.

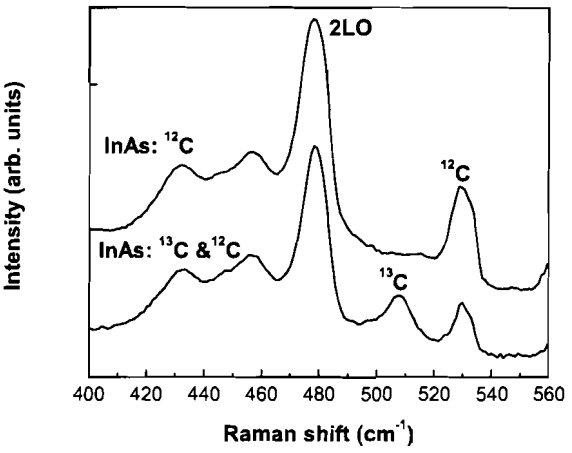

Figure 3.8: Room temperature Raman spectra of samples doped with natural carbon (^{12}C) and a mixture of isotopes (^{12}C & ^{13}C).

Table 3.2: Calculated bond lengths (Å) of C_V-III in semiconductors and bond strengths of Metal-CH_3

Semiconductor	C_V-III bond length (Å)	III-CH_3 bond strength (kcal/mole)
AlAs	1.99	66
AlSb	2.01	66
GaP	1.95	59
GaAs	1.96	59
GaSb	1.99	59
InP	2.10	47
InAs	2.12	47

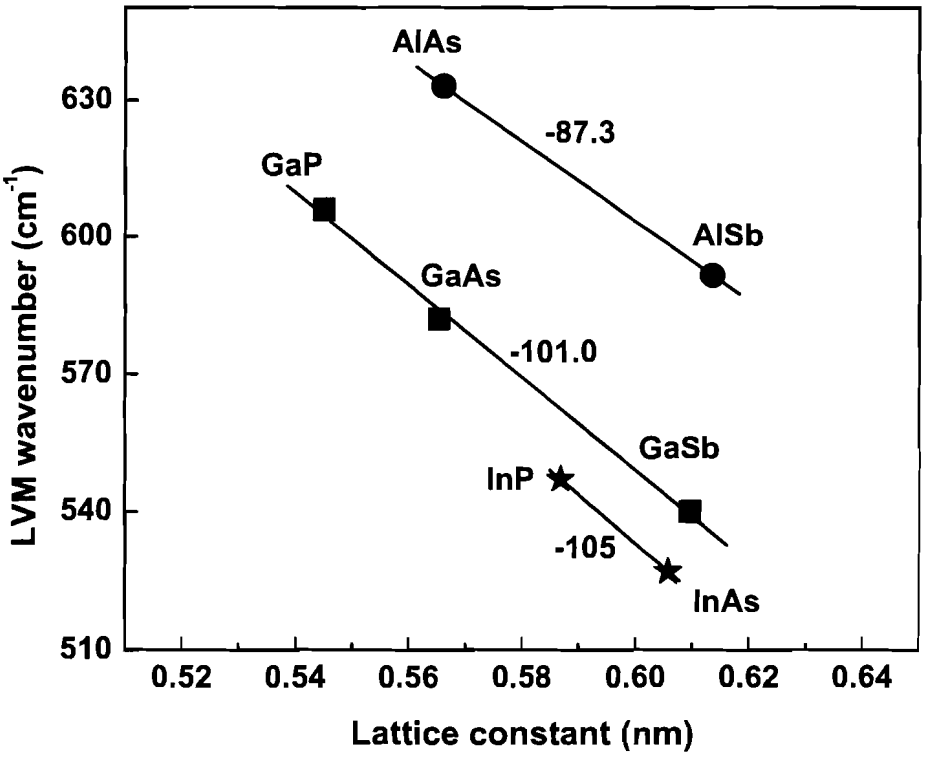

Figure 3.9: The LVM wavenumber of C_V vs lattice constant for several III-V semiconductors. The slopes of the fitted lines have been written on each line.

Although these bond strengths are not the exact values for the C_V-III values in semiconductors, they nevertheless indicate the relationship among them. For each class, a softening of the LVM energy is observed as the covalent radius of the group V atom increases and so does the lattice constant of the material. The fact that the energy of the detected carbon LVM in InAs follows the same trend as the carbon acceptors in the other semiconductors, indicates that isolated carbon is most likely a substitutional acceptor in InAs; however, more spectroscopic results will be used to confirm this assignment.

In figure 3.10 , we compare the Raman spectra of a carbon-doped sample grown at 375 °C before and after being annealed at 400 °C for 30 min in nitrogen ambient. The reduction of the intensity of the line observed at 386 cm^{-1} along with an increase

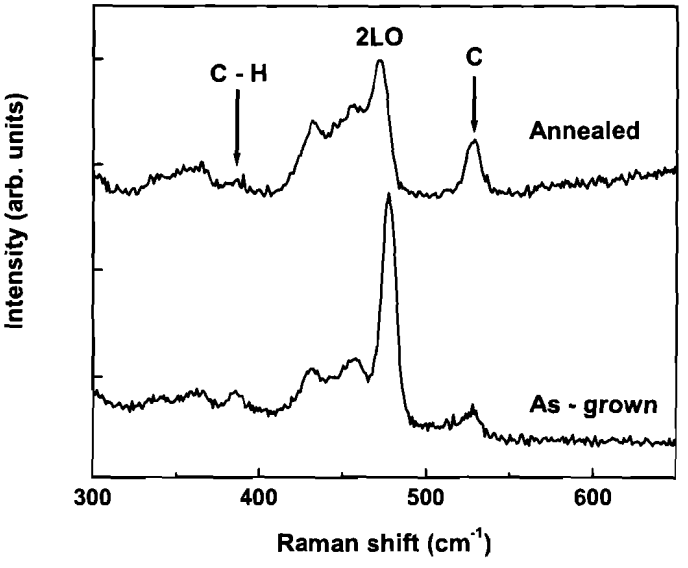

Figure 3.10: Raman spectra of a InAs:C sample before and after being annealed at 400°C in N_2.

of the carbon line strength suggests that this LVM should be related to a carbon-hydrogen complex. Similar peaks have been detected for carbon doped GaAs and InP

at 452.7 and 413.5 cm^{-1} , respectively, and have been attributed to the $A_1{}^+$ mode of C_V-H complexes [51, 27]. This will be discussed in more detail after introducing the IR absorption results.

3.3.2 Infra-red absorption by isolated carbon impurities

IR absorption measurements were performed by professor Thewalt's group at Simon Fraser University with a Bomem DA8 interferometer using a Mylar beamsplitter and a Si:B detector at 4.2 K for the low energy modes and a CaF_2 beamsplitter and InSb detector at 77 K for the higher energy modes. For both sets of measurements, the samples were cooled by flowing He gas in a Varitemp Dewar, with polypropylene windows for the low-energy measurements and ZnSe windows for the high-energy region. Samples were grown to an approximate thickness of 1 μm to maximize the absorption signal. The absorbance of the samples is not calibrated.

Figure 3.11 shows our results of IR absorption measurements of the InAs samples doped with natural carbon ($\sim$ 99% of ^{12}C) and a mixture of isotopes ($\sim$ 70% of ^{13}C and $\sim$ 30% of ^{12}C) at T=25 K in the low energy region.

The strong peak in the spectrum of the InAs:^{12}C at 530 cm^{-1} is the isolated carbon LVM that was previously detected by Raman spectroscopy. The 3 cm^{-1} shift towards higher energy is due to the lower measurement temperature. The spectrum of the sample doped with both isotopes shows the same LVM together with another one at 511 cm^{-1} arising from ^{13}C. The ratio of the integrated absorption of these two modes is approximately 30:70 consistent with their abundances in the CCl_4 source. Theoretical calculations using ab-initio density functional code have been recently reported by Torres *et al.* [52] for LVM energies of carbon acceptors and donors in InAs. According to their results, carbon acceptors and donors give rise to LVMs at 502 cm^{-1} and 439 cm^{-1} , respectively with the isotopic shifts of 19 cm^{-1} and 16 cm^{-1} . The calculated LVM energy of carbon on the As lattice site and its isotopic shift are very close to our measured value and this confirms our attribution of this peak to carbon acceptors. The other peaks labeled as C_{As}-H (E-mode) and "? " will be discussed later in this chapter.

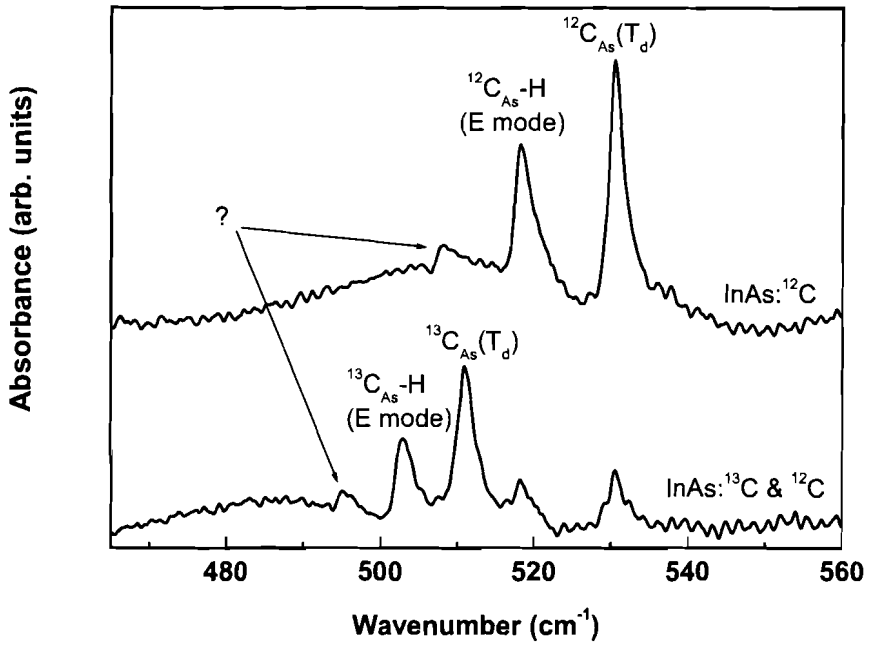

Figure 3.11: IR absorption spectra of InAs:C samples doped with ^{12}C and a mixture of both isotopes. Labels will be explained later.

3.3.3 Hydrogen passivation of carbon impurities in InAs

The incorporation of hydrogen in semiconductors has been widely studied in different materials. Hydrogen can be introduced into semiconductor materials intentionally after growth by using techniques such as hydrogen plasma treatment. However, as a common constituent of most of the chemicals used in the epitaxial growth methods and also device processing methods, hydrogen can unintentionally be incorporated in semiconductor materials as a residual impurity and modify their doping properties. It is known that hydrogen can interact with both native defects and doping atoms by forming neutral complexes through a process called "passivation" or "neutralization"

[53]. Although this effect can sometimes be beneficial by reducing the density of electrically active dangling bonds and dislocations (for example in silicon solar cells [54]), in most cases it is an undesirable phenomenon leading to inactivation of the intentional dopants as well. Hydrogen can also be incorporated as an isolated interstitial impurity and act as a donor (H^+) or an acceptor (H^-). It is known that in most cases, it counteracts the conductivity caused by the other impurities or "compensates" them [55]. When hydrogen atoms passivate other defects, they turn the ionized impurities into neutral complexes which cause little carrier scattering. In the case of compensation, both donors and acceptors are present and each one contributes to the carrier scattering separately. Therefore, compensation can be distinguished from passivation by the lower carrier mobility of the samples. In all these cases, a detailed understanding of the characteristics of hydrogen in semiconductors is critical for improving the properties of the semiconductor devices.

Electric field drift measurements show that interstitial hydrogen ions can be present in three charge states. H^+ is predominant in p-type semiconductors while H^- and H^0 are generally found in n-type semiconductors [56]. In both types of materials the formation of H^+- or H^--dopant complexes is the result of a Coulomb attraction between the interstitial hydrogen atoms and the dopant ions with opposite charge states. The vibrations of the hydrogen atoms in these complexes result in the occurrence of local vibrational modes at frequencies higher than the lattice frequencies. Therefore, vibrational mode techniques such as IR absorption measurements and Raman spectroscopy can be employed to investigate the vibrations of hydrogen atoms as well as the modified modes of the passivated impurities.

3.3.3.1 Hydrogen passivation of acceptors

Hydrogen passivation of acceptors in III-V semiconductors has been studied widely for different kinds of materials such as GaAs:Zn [57], InP:Zn, Mg, Cd [58], GaAs:C, and AlAs:C [59]. Among these materials, carbon-doped GaAs has been studied the most both experimentally and theoretically. Since the passivation process is very similar for all these cases, we'll focus on the C-H complexes in GaAs.

The first spectroscopic evidence of the presence of C-H complexes in GaAs was found by Clerjaud *et al.* [60]. They detected a sharp line at 2635.13 cm^{-1} together with a weaker line at 2628.39 cm^{-1} with an intensity ratio of 1% in the IR spectra of the carbon doped samples. Considering the very high energy of these lines, the ratio of the intensities, which is very close to the ratio of the natural abundances of ^{13}C and ^{12}C (~1.12%), and also the frequency shift that was very close to the calculated isotopic shift of the C-H complexes, they concluded that hydrogen atoms bond directly to the carbon atoms and the vibrations of the resultant complexes give rise to the observed LVMs. The results of their measurements under uniaxial stress led them to the conclusion that the observed lines were the stretch modes of the C-H bonds aligned along the trigonal axis of the crystal (in which C and H oscillate out of phase). All of these observations can be summarized in a picture showing the structure of this defect schematically (Figure 3.12).

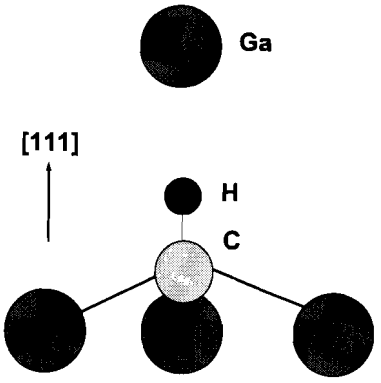

Figure 3.12: Schematic representation of the C-H structure.

In addition to the A_1 stretch mode, these complexes have three other vibrational modes: a longitudinal mode (453 cm^{-1}) due to the in-phase oscillations of carbon and hydrogen atoms, an antisymmetric E^- mode (739 cm^{-1}) arising from the out of phase transverse motion, and the symmetric E^+ mode (562.6 cm^{-1}) of the in-phase transverse oscillations [51]. All of these modes except the E^- one were detected by

IR spectroscopy and the latter one was later detected by Raman spectroscopy [61]. The absence of the E^- mode from the IR absorption spectra was explained by the weak induced dipole moment calculated by the theoretical methods [62]. The relative displacements of carbon and hydrogen atoms for different vibrational modes of the C-H complexes are shown in figure 3.13.

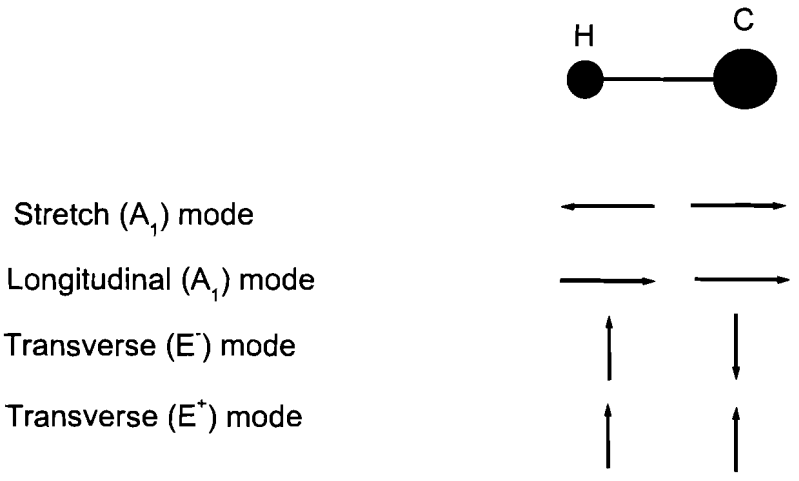

Figure 3.13: Relative displacements of the atoms in the C-H complexes.

C-H centers are not the only hydrogen-related defects in GaAs. For the highly doped samples three other vibrational modes have been detected at 2643, 2651, and 2688 cm^{-1} [63]. It is believed that those are due to the other carbon-hydrogen complexes such as $(C_{As})_2H$ and $(C_{As})_2H_2$. Cheng *et al.* [64] performed polarization dependent IR absorption measurements on highly carbon-doped GaAs samples. The lines at 2643 and 2651 cm^{-1} didn't show any preferred polarization whereas the one at 2688 was strongly polarized along the [110] crystallographic direction. Their proposed model for this defect is schematically shown in figure 3.14. To our knowledge, these high frequency carbon-hydrogen stretch modes have been detected only in highly doped GaAs and InP.

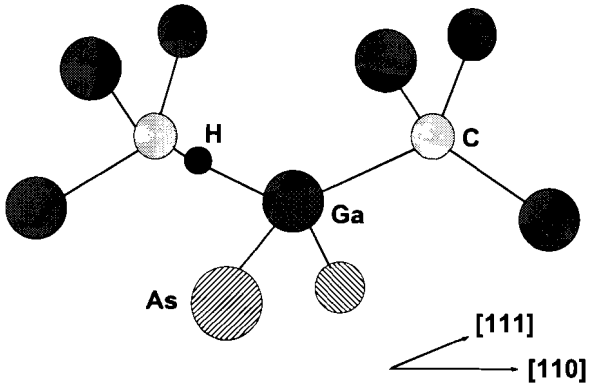

Figure 3.14: Schematic representation of the $(C_{As})_2H$ structure.

3.3.3.2 Hydrogen passivation of donors

It is believed that due to the higher diffusivity of the hydrogen atoms in p-type materials compared to that of n-type materials, hydrogen passivation of acceptors is more common than the passivation of donors [65]. Also the passivation mechanism of the donors in III-V semiconductors is more complicated than the passivation of the acceptors. For group VI donors occupying the As lattice sites in GaAs, hydrogen atoms are believed to locate at the antibonding sites close to the neighboring Ga atoms, where they are not directly bonded to the donor atoms [66]. In contrast, amphoteric group IV donors replacing the Ga lattice sites in GaAs, become passivated by hydrogen atoms residing on antibonding positions where they are directly bonded to the donor atoms (Figure 3.15) [67]. In both cases the donor-hydrogen complexes give rise to two LVMs: a high frequency stretch mode and a wagging mode (1717.3 cm^{-1} and 896.8 cm^{-1} respectively for GaAs:Si_{Ga}). The relatively lower frequencies of these modes compared to the acceptor-hydrogen ones (2095 cm^{-1} for Si_{As}-H [68]) indicate the lower bond strengths of these complexes.

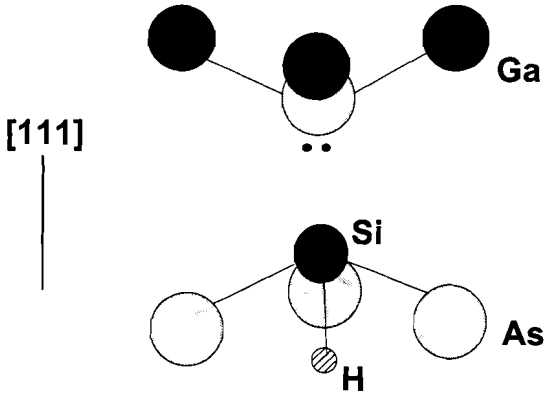

Figure 3.15: Schematic representation of the Si_{Ga}-H structure in GaAs.

3.3.3.3 Carbon-hydrogen complexes in InAs

In this section we present our results of the IR absorption measurements that led to the detection of the C-H LVMs in InAs. Also we discuss the lattice sites of the carbon atoms in InAs based on the hydrogen passivation of these defects.

Figure 3.16 shows the IR absorption spectra measured at T=25 K in the wavenumber region of 2650 to 2840 cm^{-1} for two sets of samples: one doped with natural carbon (99% ^{12}C) and the other doped with two isotopes of carbon (70% ^{13}C and 30% ^{12}C). The strong peak of spectrum (a) at 2686.5 cm^{-1} appears weaker in spectrum (b) together with another line at the wavenumber of 2678.8 cm^{-1} . The ratio of the integrated absorptions of these two lines in spectrum (b) is 2.12 that is very close to the ratio of the abundances of two isotopes in the CCl_4 source (70/30 = 2.33). This clearly shows that carbon atoms are involved in the defects that give rise to these vibrational modes. On the other hand the high frequency of the LVMs is a sign of the presence of hydrogen atoms. All these facts together with the closeness of the frequencies of these modes to the stretch modes of C_V-H in other III-Vs such as GaAs (2635.2 cm^{-1}) and InP (2703.3 cm^{-1}) and C-H bonds in organic compounds (~2800 cm^{-1}) leads to the conclusion that these LVMs are the stretch modes of the vibrations of ^{12}C-H and ^{13}C-H complexes.

In figure 3.17 we show the frequencies of the C-H stretch modes as a function of

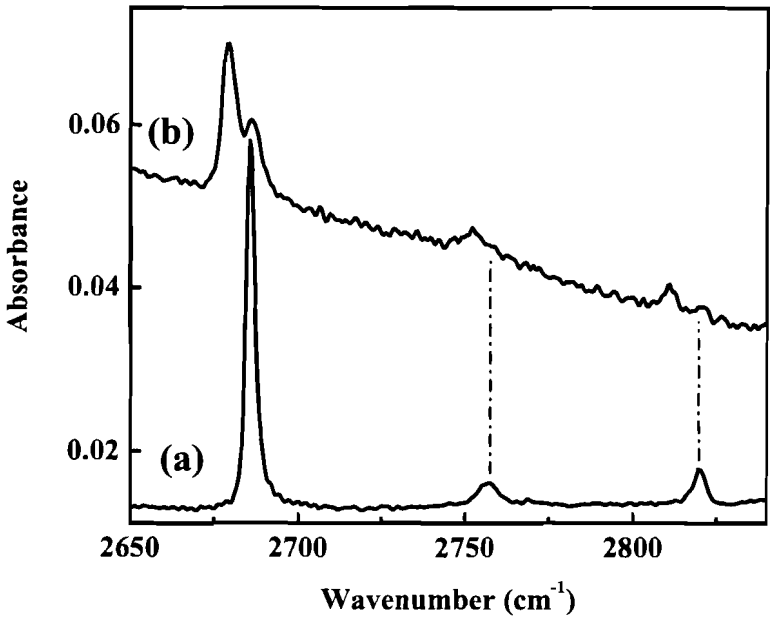

Figure 3.16: IR absorption spectra of InAs samples doped with (a) natural carbon and (b) both isotopes of carbon.

the lattice constants of different III-V semiconductors. Similar to figure 3.9, there are three different categories, each containing materials with the same group III atoms. Unlike carbon LVMs, the frequency of the C-H complexes increases with increasing covalent radius of the group III atoms. This can be explained by the bond strengths of the hydrogen atoms with the neighboring atoms. Hydrogen atoms have strong bonds with the carbon atoms and relatively weaker interactions with the group III atoms ([51]). The strength of the III-H interactions reduces by increasing the radius of the group III atoms and this leads to the stronger C-H bonds and consequently the higher LVM frequencies. For the In and Ga-containing materials the LVM wavenumber decreases by increasing the lattice constant but AlAs and AlSb do not show the same trend and their frequencies are very close together.

In addition to the C-H stretch mode, two other lines appear in these spectra at

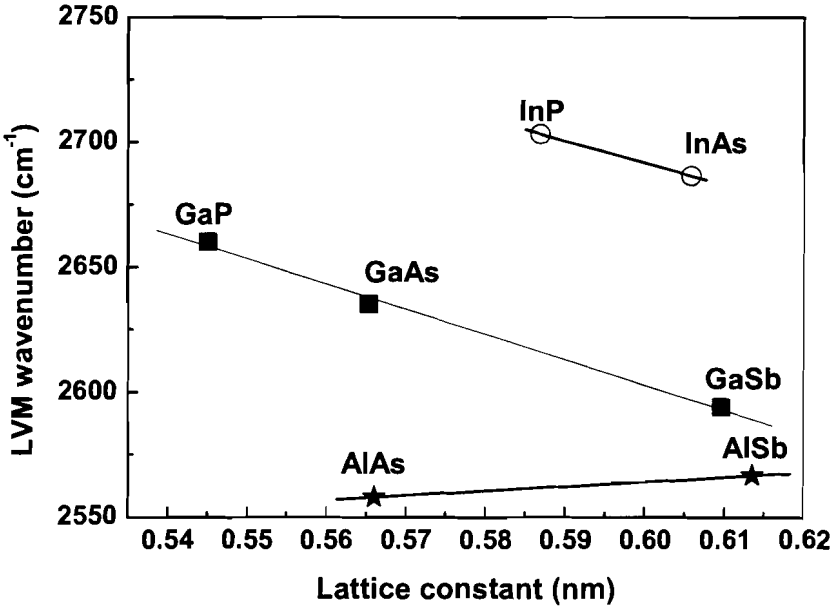

Figure 3.17: LVM wavenumber of C_V-H vs lattice constant for several III-V semiconductors.

2756.9 and 2819.6 cm^{-1} with isotopic separations of 5 and 8.6 cm^{-1} . These lines are similar to the LVMs arising from $(C_{As})_2H$ and $(C_{As})_2H_2$ complexes for highly carbon-doped GaAs mentioned in section 1.3.3.1. For carbon-doped InP these complexes have been detected at almost the same frequencies as InAs (2756 and 2818 cm^{-1}).

In section 1.3.1 we mentioned that the room temperature Raman spectra of InAs:C samples included an LVM at 386 cm^{-1} and considering that it became very weak after annealing the sample in the nitrogen ambient, we assumed that it should be related to some kind of carbon-hydrogen complex. This mode was detected by IR absorption measured at T= 25 K at the wavenumber of 393.2 cm^{-1} with the isotopic separation of 13.5 cm^{-1} (Figure 3.18). The isotopic frequency shift for this line (393.2/379.7=0.966) is very close to the square root of the mass ratio of ^{12}C-H/^{13}C-H (=0.964). Considering this fact together with the closeness of the frequency of this line to the frequency of

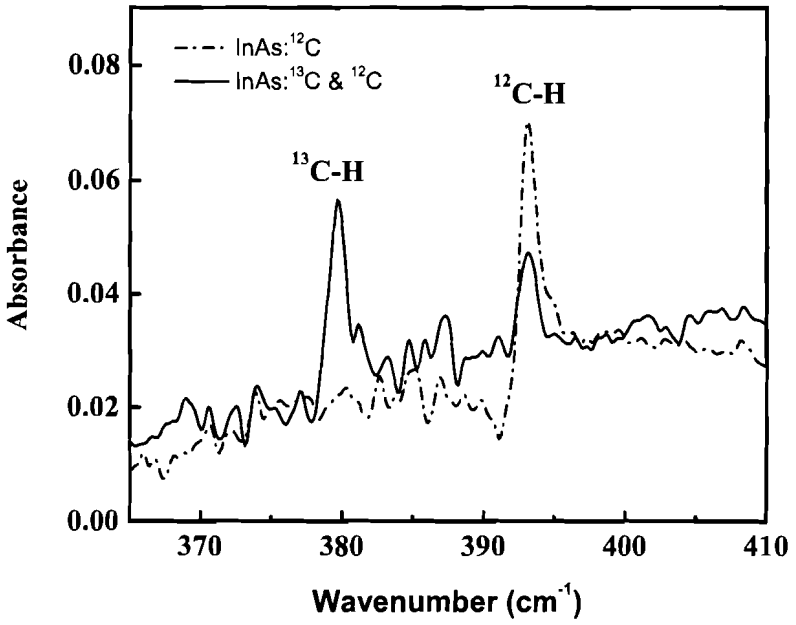

Figure 3.18: IR absorption spectra showing the A_1 longitudinal mode of ^{12}C-H and ^{13}C-H.

the longitudinal A_1 mode of the C_V-H complex in GaAs (452.7 cm^{-1}) [51] and InP (413.5 cm^{-1}) [27], we assigned this line to the low frequency longitudinal mode of the C-H vibrations in which both atoms oscillate in phase.

In figure 3.11, in addition to the LVMs of the isolated carbon atoms, two other modes appear at 518.2 and 508 cm^{-1} with isotopic separation values of 15.4 cm^{-1} and 12.8 cm^{-1} , respectively. The wavenumber and the isotopic separation of the mode at 518.2 cm^{-1} are very close to the corresponding values for the E^+ mode of the C_V-H complexes in GaAs ([51]) and InP ([27]). Therefore, we attributed this line to the E^+ mode of the C-H complexes in InAs.

In table 3.3, we have summarized all the C and C-H LVM frequencies for InAs:C along with those for GaAs:C and InP:C. We were not able to identify the line at 508 cm^{-1} . The possibility of assigning this line and the one at 518.2 cm^{-1} to the carbon

Table 3.3: C and C-H LVMs of InAs, GaAs, and InP

	LVM frequency (ω) (cm^{-1})			Isotopic separation $\omega(^{12}C)$-$\omega(^{13}C)$		
Mode	InAs (20 K)	InP (10 K)	GaAs (10 K)	InAs	InP	GaAs
^{12}C	530	546.9 [a]	582.8 [c]	19	20.1	21
H-$^{12}C(A_1^+)$	393.2	413.5 [a]	452.7 [c]	13.5	-	14.9
H-$^{12}C(E^+)$	518.2	521.1 [a]	562.6 [c]	15.4	-	15
H-$^{12}C(A_1^-)$	2686.5	2703.3 [a]	2635.2 [c]	7.7	6.7	6.7
H-$^{12}C_2$	2756.9	2756 [b]	2688 [d]	5	-	-
H_2-$^{12}C_2$	2819.6	2818 [b]	2725 [e]	8.6	-	-

[a]Ref. [27]
[b]Ref. [38]
[c]Ref. [51]
[d]Ref. [64]
[e]Ref. [69]

donors occupying the In lattice site was ruled out using equation 2.18, because it resulted in the unacceptable values of 0.3 and 0.5 respectively for the χ parameter. Also it will be shown in the next chapter that this peak disappears after annealing the samples in a TBAs environment. This could not be explained if the line was due to carbon donors. There is a possibility that the unknown line is due to the transverse mode of the carbon atom in the $(C_{As})_2H$ and $(C_{As})_2H_2$ complexes. A similar line has been observed for the highly doped GaAs:C at 576 cm^{-1} [70]. Considering the correlation between the intensity of this LVM with the combined intensities of the $(C_{As})_2H$ and $(C_{As})_2D$ lines, Davidson *et al.* suggested the attribution of this LVM to the transverse mode of carbon in these complexes. In the case of InAs, more investigation is needed to validate this assumption. The other possibility has been proposed by the recent theoretical work of Torres *et al.*(private communication). They have shown that a carbon atom at the As lattice site bonded to two hydrogen atoms at the bond center positions is an energetically favorable configuration. According to the their calculations, a structure like this can give rise to a LVM energy close to the one in our measurements.

As we discussed in section 1.3.3.2, donor-hydrogen complexes with the hydrogen atoms locating at the antibonding positions, give rise to two LVMs: one stretch mode and one wagging mode. The presence of three different modes of C-H vibrations for InAs shows that hydrogen atoms occupy the bond-center positions and are directly bonded to the carbon atoms. This fact together with the closeness of the LVM frequencies to those of the C_V-H complexes in other materials provide strong support for the idea that isolated carbon atoms occupy the As lattice sites in InAs and become acceptors.

3.3.4 Dicarbon complexes in carbon-doped InAs

Although in highly carbon doped GaAs samples, most of the carbon atoms occupy the As lattice sites and become acceptors, it has been known that there is a discrepancy between the total concentration of the carbon atoms in the samples and the hole concentration [47]. Annealing the samples at high temperatures (~800°C) not only

increases the discrepancy between the carbon and the hole concentrations, but also decreases the lattice mismatch between the doped and the undoped materials [39]. The compensation of the carbon acceptors could be caused by the site switching of the carbon atoms to the Ga lattices sites; however, there has been no spectroscopic evidence for the presence of the carbon atoms on the Ga sites. Also the site switching would not affect the lattice constant because of the similar covalent radii of As and Ga atoms. Hydrogen passivation of the acceptors can be partly responsible, although even the samples grown by chemical beam epitaxy with low amounts of hydrogen showed the same thermal instability [71].

An alternative explanation for this reduced electrical activity at high doping levels and after annealing, is the diffusion of carbon atoms to interstitial sites. According to theoretical studies using the first-principal pseudopotential method, interstitial carbon atoms that act as double donors are not stable defects and can be trapped by C_{As} to form C-C complexes [40]. These calculations showed that the most stable form of the dicarbon defects is the split interstitial pair located at an As site, aligned along the [100] direction. Since two carbon atoms occupy an As lattice site, the amount of lattice contraction decreases by the formation of these defects. Cheong *et al.* also suggested a formation process for the dicarbon complexes. They calculated an activation energy of 0.7 eV for the diffusion of carbon acceptors to interstitial sites. This energy barrier can be decreased by assuming that substitutional carbon atoms are kicked out of their sites by interstitial As atoms through the following reaction:

$$C_{As} + As_i \rightarrow As_{As} + C_i \tag{3.6}$$

The reduction of the strain energy as a result of the occupation of the As lattice sites by As atoms leads to a lower energy barrier for the diffusion of the carbon atoms.

The charge states of the dicarbon defects in GaAs and AlAs have been investigated by Jones *et al.* using first principles local density functional cluster theory [72]. According to their results, C_{As}-C_i defects are donors and have energy levels deep inside the gap. For AlAs, they predicted an IR-inactive stretch mode at 1590 cm^{-1} and another mode at 433 cm^{-1} .

The first spectroscopic evidence of the existence of the dicarbon defects was reported by Wagner *et al.* for highly carbon doped GaAs samples annealed at 850°C [39]. Two Raman LVMs were detected at 1742 (T1) and 1859 cm^{-1} (T2) that were attributed to dicarbon centers. The presence of two triplet structures in the Raman spectra of the samples doped with equal concentrations of ^{12}C and ^{13}C with the relative strengths of 1:2:1 was used to make this assignment. The symmetry of the defects was determined to be A_1 considering the fact that the intensity of both lines was higher for the parallel rather than perpendicular polarizations of the incident and the scattered light. Similar LVMs were observed for annealed carbon-doped AlAs samples at the wavenumbers of 1743 (T1) and 1856 cm^{-1} (T2) [73]. In both cases the T1 mode had a greater strength than the T2 one but the ratio of the intensities was almost the same for the samples with different carrier concentrations. Therefore it was concluded that both lines arose from the same defect.

Davidson *et al.* performed ab initio calculations using a density functional cluster model to understand the structure of the dicarbon defects [73]. They found that the induced dipole moment of the C-C stretch mode was almost zero and therefore the mode was IR-inactive. The defect can have other modes at frequencies below 500 cm^{-1} but they were not detected for AlAs or GaAs. According to their model, the energy levels of the dicarbon defect aligned along the [110] direction (C_{2v} symmetry) and the one aligned along the [111] direction (C_{3v} symmetry), are 0.5 eV lower than the one along the [100] direction predicted by Cheong *et al.* [40]. Therefore, dicarbon defects aligned along [111] and [110] directions are more stable than those along [100] direction. They attributed the T1 and T2 lines to dicarbon defects in these two stable configurations; however, due to the uncertainties in their calculations, it was not possible to distinguish between the T1 and T2 lines.

A schematic representation of the split interstitial $(C\text{-}C)_{As}$ defects in GaAs aligned along three different directions is shown in figure 3.19.

Raman scattering measurements of as-grown InP:C samples revealed the existence of dicarbon defects in this material [38]. Two LVMs at 1784.9 and 1814 cm^{-1} were detected, with the greater intensity for the latter one. It was concluded that these deep donors can be partly responsible for the compensation of the carbon acceptors;

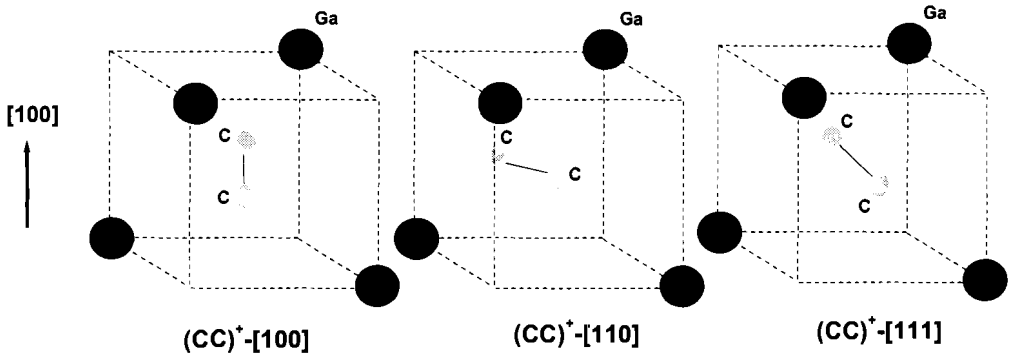

Figure 3.19: A schematic representation of the C-C defect aligned along the [100], [110], and [111] directions of the GaAs lattice.

however, the possibility of the presence of the other donor species such as C_{In} and $V_{In}H_4$ were not excluded.

3.3.4.1 Raman scattering by dicarbon defects in InAs:C

We showed in the previous sections that the results of our spectroscopic measurements provided enough evidence that carbon atoms in InAs occupy the As lattice sites and become acceptors similar to the other III-V semiconductors. Although these acceptors are highly passivated by hydrogen atoms, the high concentration of the carbon atoms deduced from the SIMS measurements and the n-type conductivity of the samples shows that high concentrations of compensating donor defects are present.

We conducted Raman scattering measurements in the frequency region around 1800 cm^{-1} to look for dicarbon centers in our samples. Figure 3.20 shows the spectra for two sets of samples: one doped with natural carbon (99% ^{12}C) and the other doped with a mixture of two isotopes (70% ^{13}C and 30% ^{12}C). The spectrum of the sample doped with ^{12}C shows a broad line at 1832 cm^{-1} . A triplet structure was

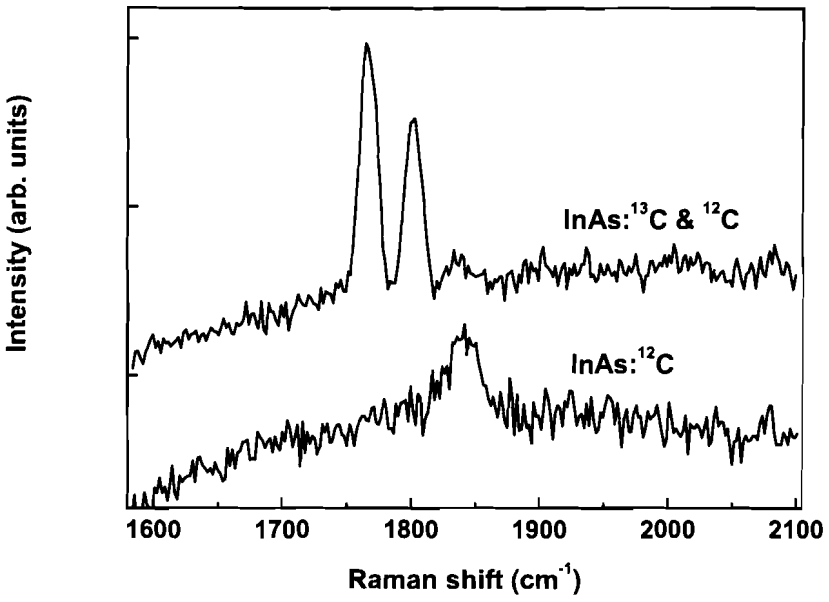

Figure 3.20: Raman scattering by dicarbon defects in InAs

detected in the spectrum of the other sample with LVM energies of 1758, 1794, and 1832 cm^{-1} . These lines were assigned to the stretch modes of ^{13}C-^{13}C, ^{13}C-^{12}C, and ^{12}C-^{12}C complexes in comparison with other III-Vs such as GaAs and InP. The ratio of the mode energies of ^{12}C-^{12}C to ^{13}C-^{13}C is 1.042, compared to $(13/12)^{0.5}$=1.041. Considering the abundances of the two isotopes in the CCl_4 source, the probability of having ^{13}C-^{13}C, ^{13}C-^{12}C, and ^{12}C-^{12}C bonds is 5.4 : 4.7 : 1. The ratio of the area under the three peaks in the spectrum is 5.9 : 4.0 : 1, respectively. The closeness of these ratios confirms these assignments.

The fact that the dicarbon LVMs can be detected in as-grown InAs and InP [38], reveals that the concentration of the dicarbon defects in these materials is high even for the as-grown samples. This demonstrates an important difference between these two In-containing materials and other III-V semiconductors such as GaAs, in which C-C centers do not form unless samples are annealed at temperatures higher than

800 °C. This is related to the strength of C_V-III bond (table 3.2). The higher bond strengths of Al-C and Ga-C result in the lower diffusion coefficient of the carbon impurities in AlAs and GaAs relative to those of InAs and InP. This explains the ease of dicarbon formation in InP and InAs, which requires the diffusion of carbon atoms into interstitial sites.

Chapter 4

Thermal stability of carbon in InAs

Semiconductor device fabrication processes often involve high temperature treatments such as rapid thermal annealing that can induce serious problems in the device performance by degrading the material properties. Therefore it is very important to study the thermal stability of the materials and understand the mechanism of the changes of their characteristics under the annealing conditions. The electrical activity of impurities in semiconductors is one of the most important parameters determining the performance of the devices. Therefore studying the thermal stability of impurities has been of interest for many researchers.

4.1 Thermal stability of carbon dopants in III-V semiconductors

Although carbon has been a favorable p-type dopant for many III-V semiconductors because of its lower diffusivity compared to Be and Zn, the electrical and structural properties of carbon doped materials change at high temperatures. Watanabe *et al.* [74] observed that the carrier concentration and the mobility of the highly doped GaAs:C samples decreased after annealing at temperatures higher than 600°C. They detected a deep photoluminescence peak for the as-grown samples and observed that its intensity increased after annealing at 850°C. Since this feature was not present in

the PL spectra of the lightly-doped samples, they concluded that it was caused by carbon-related defects. Although they could not determine the identity of these deep levels, they mentioned that the existence of these compensating centers explains the changes of the carrier concentration and the mobility.

Enquist *et al.* [75] reported that for carbon concentrations above 10^{20} cm^{-3} , tensile strain was relieved by annealing. They suggested three different mechanisms for the thermal instability of the GaAs:C samples: the formation of misfit dislocations, site switching of the carbon atoms from the As sites to the Ga sites, and the existence of high concentrations of the hydrogen atoms. The formation of misfit dislocations usually happens for the samples thicker than the critical thickness. However, the increase in resistivity and the strain release after the anneals were observed for samples with much lower thicknesses. Therefore, it could not be an acceptable explanation for all these changes. The idea of carbon site switching could not explain the significant change in the lattice constant because of the similar covalent radii of the As and Ga atoms. Finally hydrogen atoms were present in both as-grown and annealed samples according to SIMS measurement and their role in the thermal instability was not clear.

Westwater *et al.* [76] detected carbon clusters in highly doped GaAs:C samples annealed at temperatures around 850°C by transmission electron microscopy (TEM). They proposed that the reduction of the carrier concentration, mobility, and lattice mismatch between the layers and the undoped substrate of the annealed samples was the result of the movement of the carbon atoms to the interstitial sites. Similar kinds of effects have been reported for AlGaAs:C [77] and InGaAs:C [78].

4.1.1 Formation of dicarbon defects by annealing

It has been shown that annealing GaAs:C and AlAs:C samples with doping levels higher than 10^{20} cm^{-3} at high temperatures ($\sim$ 800 °C), results in a reduction in the hole concentration [39, 73]. This reduction is accompanied by a decrease of the lattice mismatch between the doped and the undoped samples. Raman spectroscopy of these samples showed that the intensity of the carbon LVMs decreased following the anneals

at high temperatures. Meanwhile, local vibrational modes of dicarbon defects aligned along the <110> and <111> directions were detected at 1742 (T1) and 1859 cm^{-1} (T2) for GaAs [39] and 1743 and 1856 cm^{-1} for AlAs [73], where for both materials T1 was stronger than T2. Due to the uncertainties in the theoretical calculations, the exact assignment of the T1 and T2 modes was not possible. A similar effect was observed for carbon-doped InP samples [38]. Two dicarbon LVMs at wavenumbers of 1784.9 (T1) and 1814 (T2) cm^{-1} were detected for as grown samples that became stronger by annealing the samples up to 800 °C. A third line at 1763.7 cm^{-1} appeared after annealing. In contrast to GaAs and AlAs, the strength of the T2 mode was higher than that of the T1 mode in this case.

All these changes were explained by the formation of dicarbon complexes (the mechanism was explained in section 3.3.4). Since these defects are deep donors according to theoretical calculations [72], they compensate the isolated carbon acceptors and this results in the reduction of the hole concentration in the case of GaAs and AlAs.

4.1.2 Dissociation of carbon-hydrogen complexes by annealing

Although annealing at very high temperatures ($\sim$ 800°C) causes undesirable changes in the properties of the semiconductor materials, annealing at moderate temperatures ($\sim$ 500°C) can be beneficial in reactivating passivated dopants. Annealing at these temperatures in a non-hydrogen ambient such as N_2 or He has been widely used to diffuse the hydrogen atoms out of the samples and reactivate the dopants. Kozuch *et al.* measured the thermal stability of the C-H and C_2-H complexes by annealing carbon-doped GaAs samples in He at different temperatures and measuring the strength of the IR stretch modes of the complexes [63]. They found that the intensity of the C-H stretch mode at 2636 cm^{-1} was almost zero for the samples annealed at temperatures around 500 °C; however the mode arising from the C_2-H complexes at 2688 cm^{-1} was more stable and did not disappear until 600 °C. This was consistent

with the results of the theoretical calculations of Cheng *et al.* [64]. A similar observation has been reported by Mimila-Arroyo *et al.* who studied the changes of the IR stretch modes of the carbon-hydrogen complexes for the samples annealed at 600 °C for different durations of time [79]. According to that work, the dissociation of the C_2-H bonds took a longer time than that of the C-H bonds. They also observed that in spite of the C-H complexes that their dissociation resulted in an increase in the hole concentration, the decomposition of the C_2-H complexes did not cause any change in the electrical properties of the materials. Considering this together with the higher bonding energy between hydrogen atoms and C_2, they concluded that C_2 (two carbon atoms occupying two neighboring As sites) must be a deep acceptor that does not ionize at room temperature.

4.2 Annealing carbon-doped InAs samples

In this section we present a study of the effects of annealing on the characteristics of carbon-doped InAs samples and discuss the mechanism of the changes.

InAs samples grown at 375°C with a carbon precursor flow rate of 1.31 μmole/min were annealed inside the OMVPE reactor in a TBAs ambient at temperatures of 400, 500, 600, and 680 °C following the growth. The thickness of the samples was determined to be 180 nm by XRD measurements. Two one-micron thick samples were also annealed at 600 °C in TBAs ambient for the IR absorption measurements. The effects of annealing on the electrical, structural, and vibrational properties of the samples were studied by Van der Pauw Hall measurements, XRD, Raman spectroscopy, and IR absorption measurements.

4.2.1 Raman and IR spectroscopy of the annealed samples

Raman spectroscopy was performed on the as-grown and the annealed samples in the frequency range of the carbon acceptors and dicarbon complexes. Most of the measurements were done using unpolarized laser light.

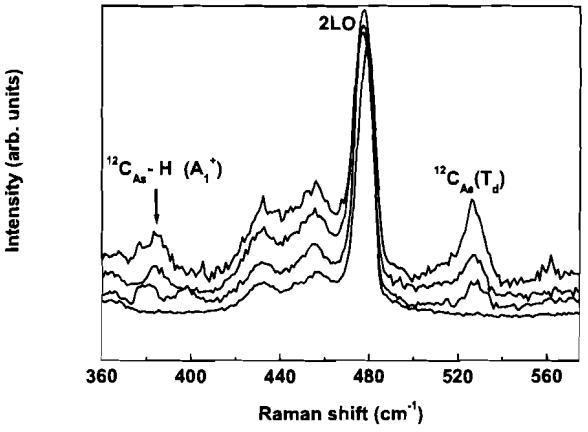

Figure 4.1: Raman spectra of as-grown and annealed samples at 400, 500, and 600°C from top to bottom. The 2LO line was used for normalization.

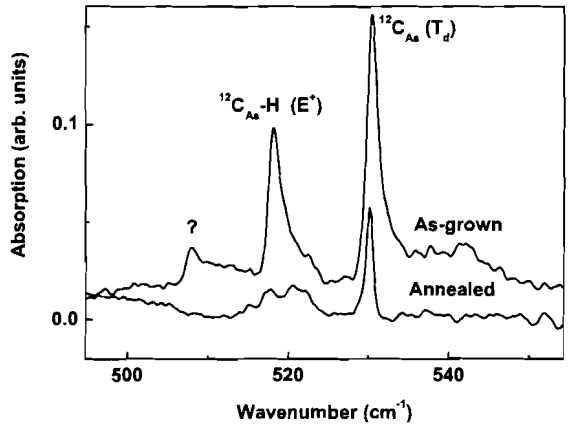

Figure 4.2: IR absorption spectra of the as-grown and the annealed samples at 600°C. The absorption axis is not calibrated.

Figure 4.1 shows the Raman spectra for the samples annealed at different temperatures and the as-grown one in the frequency range of 360 to 575 cm^{-1} . The intensity of the carbon LVM at 527 cm^{-1} normalized to the 2LO peak, decreased by raising the anneal temperature and became lower than the detection limit for the sample annealed at 600 °C. Although the $A_1{}^+$ mode of the C-H complexes at 386 cm^{-1} did not show the same trend, its intensity was higher for the as-grown sample compared to the annealed ones and it was lower than the detection limit for the sample annealed at 600 °C. The reduction of the intensity of the C and C-H related LVMs was observed by IR absorption measurements as well. Figure 4.2 shows the IR spectra of a one-micron thick sample before and after annealing at 600 °C in a TBAs ambient. The E^+ mode of the C-H complexes at 518 cm^{-1} and also the unknown peak at 508 cm^{-1} were not present on the spectrum of the annealed sample and the integrated absorption of the C_{As} mode decreased by a factor of 2.7 after annealing.

Figure 4.3 shows the Raman spectra for the same samples as in Fig 4.1 in the frequency range of the dicarbon complexes. The dicarbon peaks are not normalized to the 2LO line because of the absence of this line from the measured frequency range. However, the ratio of the intensity of dicarbon LVMs to carbon LVMs (present on the same spectra) was measured and the values are summarized in table 4.1. It can be seen from all the data that the reduction in the intensity of the carbon LVM by annealing is accompanied by an increase in the strength of the dicarbon LVMs.

Table 4.1: The intensity of carbon and dicarbon LVMs detected by Raman spectroscopy and their ratios.

Sample	Intensity of C LVM ([C])	Intensity of C-C LVM ([C-C])	[C-C]/[C]
As-grown	3808	913	0.24
Annealed at 400°C	4603	2119	0.46
Annealed at 500°C	2013	2802	1.39
Annealed at 600°C	652	5814	8.92

The reduction of the strength of the C_{As} and C_{As}-H LVMs clearly shows that

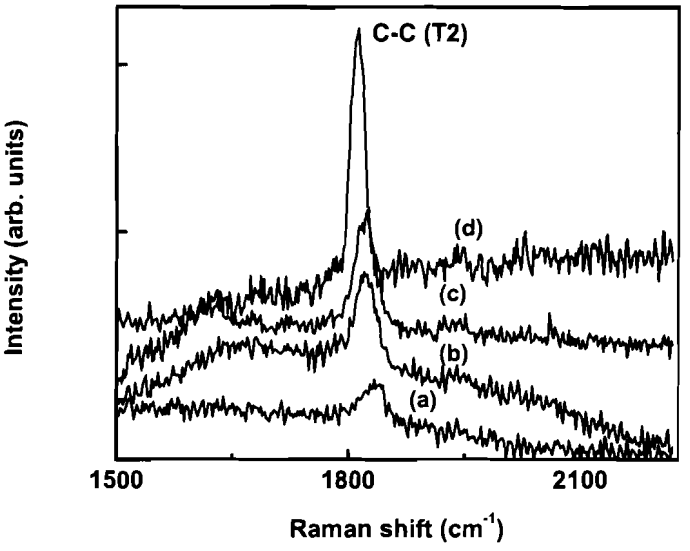

Figure 4.3: Raman spectra of InAs:C samples (a) as-grown, (b)-(d) annealed at 400, 500, and 600°C .

annealing at these moderate temperatures not only results in the dissociation of the C_{As}-H complexes, but also moves the substitutional carbon acceptors out of the As lattice sites. The possibility of site switching of the carbon atoms to the In lattice site was rejected due to the lack of any spectroscopic evidence of C_{In} donors. On the other hand, considering the increase in the intensity of the dicarbon LVMs, it can be concluded that annealing caused a precipitation of the carbon atoms in the form of C-C complexes. These defects were present in the as-grown samples (as discussed in section 3.3.4) and their concentration increased by annealing.

Similar observations have been reported for GaAs [39], AlAs [73], and InP [38]; however, there are some differences among them. In GaAs and AlAs, dicarbon LVMs can't be detected unless the samples are annealed at very high temperatures (above 800 °C), but for InP and InAs these LVMs are present even in the spectra of the as-grown samples. This was explained by comparing the bond strengths of C-III of these compounds (section 3.3.4). The other differences are the number and the relative

strengths of the dicarbon-related Raman LVMs. The strength of the higher frequency LVM of C-C (T2) in InP is higher than that of the lower frequency one (T1) which is in opposite sense to GaAs and AlAs. Also the separation between two LVMs in InP is around 25 cm^{-1} , which is lower than that for the two other materials ($\sim$ 90). For InAs, only one dicarbon LVM was detected at the frequency of 1832 cm^{-1} , which is closer to the T2 line for other materials. It can be assumed that the preferred alignment of this defect changes from one crystal direction to the other (from [111] to [110] or vice versa) for the In-containing materials. More theoretical calculations are needed to clarify this point.

Jones *et al.* had predicted an IR-active longitudinal mode for dicarbon complexes in carbon-doped AlAs at 433 cm^{-1} [72]. This mode has not been detected experimentally. The possibility of assigning the line at 508 cm^{-1} in the IR absorption spectra of InAs:C to a similar mode was ruled out because the peak did not exist in the spectrum of the annealed sample in spite of the increasing intensity of the stretch mode of the dicarbon defects. The fact that this peak disappears after annealing supports the assumption that it can be related to some kind of carbon-hydrogen complex (see section 3.3.3.3).

In order to determine the symmetry of the C-C complex, Raman measurements were conducted using two different polarization configurations for the incident and scattered light: X′ X′ and X′Y′, where X′ represents the [110] direction and Y′ the [$\bar{1}$10] direction. The first letter refers to the polarization of the scattered light and the second one to the polarization of the incident light. Results are shown in figure 4.4. No dicarbon LVM was detected in the X′Y′ configuration. In the X′ X′ polarization configuration, in addition to the line at 1832 cm^{-1}, two other lines at 1752 and 1625 cm^{-1} were observed. The last line appeared as a broad feature in the spectra of other annealed samples and not in the as-grown one. This broad band may be due to amorphous carbon formed after annealing the samples [38]. The line at 1752 cm^{-1} is similar to the T1 line detected for other materials. If this is true, the separation between the T1 and T2 lines is 80 cm^{-1} . The fact that scattering from dicarbon defects is stronger for parallel rather than crossed polarization, suggests that the line is related to the A_1 mode [39].

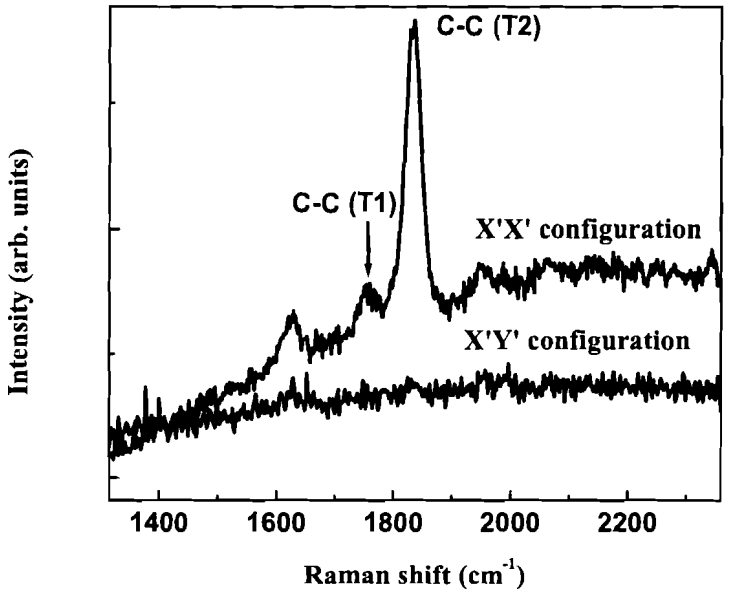

Figure 4.4: LVMs of the dicarbon complex measured with two different polarization configuration

4.2.2 Effects of annealing on the lattice parameter of the samples

XRD measurements were conducted on the as-grown and the annealed samples. The thickness of these samples was determined to be 180 nm by simulating the rocking curves using the dynamical XRD theory. Diffraction patterns are shown in figure 4.5 and the related strained lattice mismatch values are summarized in table 4.2. It can be seen that annealing at 400 °C didn't make any change in the lattice mismatch between the epilayer and the InAs substrate, but increasing the anneal temperature further resulted in a strong reduction of the lattice mismatch.

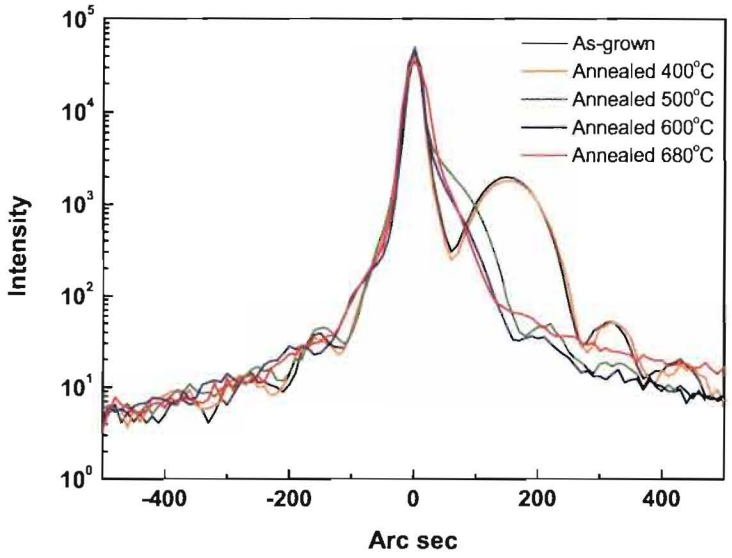

Figure 4.5: XRD patterns for as-grown and annealed InAs:C.

Table 4.2: A summary of HRXRD measurement results

Sample	$\Delta a_{\perp}/a$ (strained)	$\Delta a/a$ (relaxed)
As-grown	-1.2E-3	-5.7E-4
Annealed at 400°C	-1.3E-3	-6.0E-4
Annealed at 500°C	-2.5E-4	-1.2E-4
Annealed at 600°C	-1.6E-4	-6.3E-5
Annealed at 680°C	-1.6E-4	-6.3E-5

The lattice parameter of InAs can be affected by each of several possible carbon-related defects such as isolated carbon acceptors, carbon-hydrogen complexes, and dicarbon defects. Substitutional carbon acceptors introduce a lattice contraction due to the small size of the carbon atoms compared to the host atoms (as discussed in section 3.2). The resulting lattice mismatch can be calculated by the following equation [80]:

$$(\frac{\Delta a}{a_o})_{C,As} = \frac{4}{\sqrt{3}} \frac{r_C - r_{As}}{a_o} \frac{N_{C,As}}{N_o} \tag{4.1}$$

where $\Delta a/a_0$ is the relaxed lattice mismatch between undoped and doped InAs, r_C=0.77 $\mathring{A}$ and r_{As}=1.20 $\mathring{A}$ are the covalent radii of carbon and arsenic, a_o=6.0583 $\mathring{A}$ is the lattice parameter of the undoped InAs, and $N_{C,As}$ and N_o=1.795×10^{22} cm^{-3} are the densities of carbon acceptors and As atoms, respectively.

The lattice mismatch caused by the presence of the dicarbon and carbon-hydrogen defects in carbon-doped GaAs has been studied by Li *et al.* [80]. We used their equations to calculate the lattice mismatches caused by these defects in carbon-doped InAs:

$$(\frac{\Delta a}{a_o})_{C-C} = \frac{d_b - r_{In} - r_{As}}{r_{In} + r_{As}} \frac{C_{11} + 2C_{12}}{C_{11}} \frac{N_{CC}}{N_o} \tag{4.2}$$

where C_{11}=8.34×10^{-11} dyn/cm^2 and C_{12}=4.54×10^{-11}dyn/cm^2 are the stiffness coefficients of InAs, N_{CC} is the concentration of dicarbon centers, and d_b is the distance between the C-C defect and its nearest neighbor and can be calculated using the following equation [81]:

$$d_b = \frac{\sqrt{3}}{3} r_C + \sqrt{(r_C + r_{In})^2 - \frac{2r_C^2}{3}} \tag{4.3}$$

The lattice mismatch caused by the C-H complexes can be calculated in the same way:

$$(\frac{\Delta a}{a_o})_{C-H} = \frac{d_b - r_{In} - r_{As}}{r_{In} + r_{As}} \frac{C_{11} + 2C_{12}}{C_{11}} \frac{N_{CH}}{N_o} \tag{4.4}$$

where N_{CH} is the concentration of C-H centers and d_b is

$$d_b = \frac{\sqrt{3}}{3} r_i + \sqrt{(r_i + r_{In})^2 - \frac{2r_i^2}{3}} \tag{4.5}$$

r_i is the effective C-H bond radius equal to $(r_C+r_H)/2=(0.77 + 0.32)/2=0.545$Å. The total lattice mismatch between the carbon-doped InAs and undoped material can

be estimated by adding all these terms together. It can be stated in the following form:

$$(\frac{\Delta a}{a})_{tot} = -(9.132N_{C,As} + 8.614N_{CH} + 1.691N_{CC}) \times 10^{-18}(ppm) \qquad (4.6)$$

From equation 4.6 it can be seen that assuming equal concentrations for the defects, the contributions of C-H and C-C centers in the total lattice mismatch are 94% and 18% of that of the carbon acceptors. Therefore it can be concluded that substitutional carbon atoms and carbon-hydrogen complexes are the major species causing the observed lattice contraction. The results of Raman and IR spectroscopies confirm this conclusion by showing that the sample annealed at 600 °C has a very low concentrations of C and C-H defects and high concentration of dicarbon defects. This explains the 80 % reduction in the lattice mismatch of this sample compared to that of the as-grown one. The concentration of the dicarbon centers for the sample annealed at 680 °C can be estimated using the relaxed lattice mismatch value of table 4.2 and assuming that no C_{As} and C_{As}-H defects exist in this sample (based on the spectroscopic data of the sample annealed at 600 °C). The calculated value of N_{CC}=3.7×10^{19} cm^{-3} is close to the electron concentration of 9.8×10^{18} cm^{-3} deduced from Hall measurement of this sample. This shows that dicarbon centers are mainly responsible for the n-type conductivity of the carbon-doped InAs samples. Also, N_{CC} is close to the concentration of carbon atoms (N_C=3.5E19 cm^{-3}) measured by SIMS for the sample grown at 375 °C (Figure 3.1). This shows that most of the carbon atoms are in the form of dicarbon defects for the sample annealed at 680 °C.

4.2.3 Effects of annealing on the electrical properties of samples

Table 4.3 summarizes the electron concentration and the mobility of the as grown and the annealed samples. The concentration of electrons and their mobility increased by raising the anneal temperature, except for the sample annealed at 500 °C. Considering that the decomposition of the C_{As}-H complexes happens at temperatures of around

Table 4.3: A summary of Hall measurement results for as-grown and annealed InAs:C.

Sample	Electron Concentration (cm^{-3})	Mobility (cm^2/Vs)
As-grown	1.98×10^{18}	1820
Annealed at 400 °C	2.67×10^{18}	2328
Annealed at 500 °C	1.47×10^{18}	1881
Annealed at 600 °C	2.69×10^{18}	2366
Annealed at 680 °C	9.80×10^{18}	3146

500°C [82], we concluded that the decrease of the electron concentration after annealing at this temperature is the result of the compensation of the dicarbon donors by the reactivated carbon acceptors. According to Raman and IR spectra of samples annealed at 600 °C, C-H complexes are totally decomposed at this temperature and the concentration of the dicarbon donors increased significantly. Therefore, the high electron concentration can be explained with the high density of dicarbon donors.

Annealing the samples not only affects the electron concentrations but also affects their mobilities. Electron mobilities of the samples increase by raising the anneal temperature except for the one annealed at 500 °C. The variation of the mobilities can be mainly explained by the compensation effect. The compensating species introduce a localized potential that scatters the charge carriers. This scattering mechanism causes a reduction in the mobility [83]. By raising the anneal temperature, the concentration of dicarbon donors increases and it results in a lower compensation ratio and a higher electron mobility. The reduction of the electron mobility of the sample annealed at 500°C can be caused by the increased compensation ratio resulting from the decomposition of the C_{As}-H complexes that produced more carbon acceptors.

4.3 Annealing carbon-doped InAs samples in N_2 environment

It was previously mentioned that annealing the samples in a nitrogen ambient resulted in significant increases in the electron concentration together with dramatic drops of the electron mobility. In this section, we introduce the Hall measurement results of two samples annealed at 400 °C in a N_2 ambient for different lengths of time. Table 4.4 summarizes the thickness, electron concentration, and mobility of the as grown pieces.

Table 4.4: The as-grown properties of samples annealed in a N_2 ambient.

Sample #	Thickness (nm)	Electron concentration (cm^{-3})	Mobility (cm^2/Vs)
5059	339	1.3×10^{18}	3152
5159	75	2.2×10^{18}	3023

The samples were placed on a graphite disc that can be heated up to 400 °C by an electric heater. Nitrogen gas was flowing through the chamber during the anneal.

Figure 4.6 shows the electron concentration and the mobility of both samples as a function of the annealing time. Two stages can be distinguished in the changes of the mobility and the electron concentration. At the first stage the electron concentration shows a slight decrease that is accompanied by a dramatic reduction in the electron mobility. The annealing time for this stage is 5 min for the thinner sample (#5159) and 25 min for the thicker one (#5059). After this the electron concentration increases and the mobility decreases gradually to some saturation values after ~175 min for the thinner sample and ~965 min for the thicker one.

The fact that the samples annealed in a TBAs ambient and at temperatures even higher than 400 °C did not undergo similar changes, suggest that the desorption of As atoms from the surface is responsible for the observed behavior. It is possible that the electrical transport of these samples is the result of conduction in two layers: a

surface layer resulting from As desorption and a bulk layer. By increasing the anneal time, the thickness of the surface layer increases and consequently its contribution in the transport properties of the samples increases. This results in the observation of high electron concentrations and very low mobilities.

Raman spectrum of a sample annealed in a N_2 ambient is shown in figure 3.10. It can be seen that annealing in a N_2 ambient has the same effect on the concentration of C-H complexes as annealing in a TBAs ambient. This confirms that the bulk properties of the samples annealed in a N_2 ambient are the same as those annealed in a TBAs ambient and Hall measurements results are affected by surface degradation.

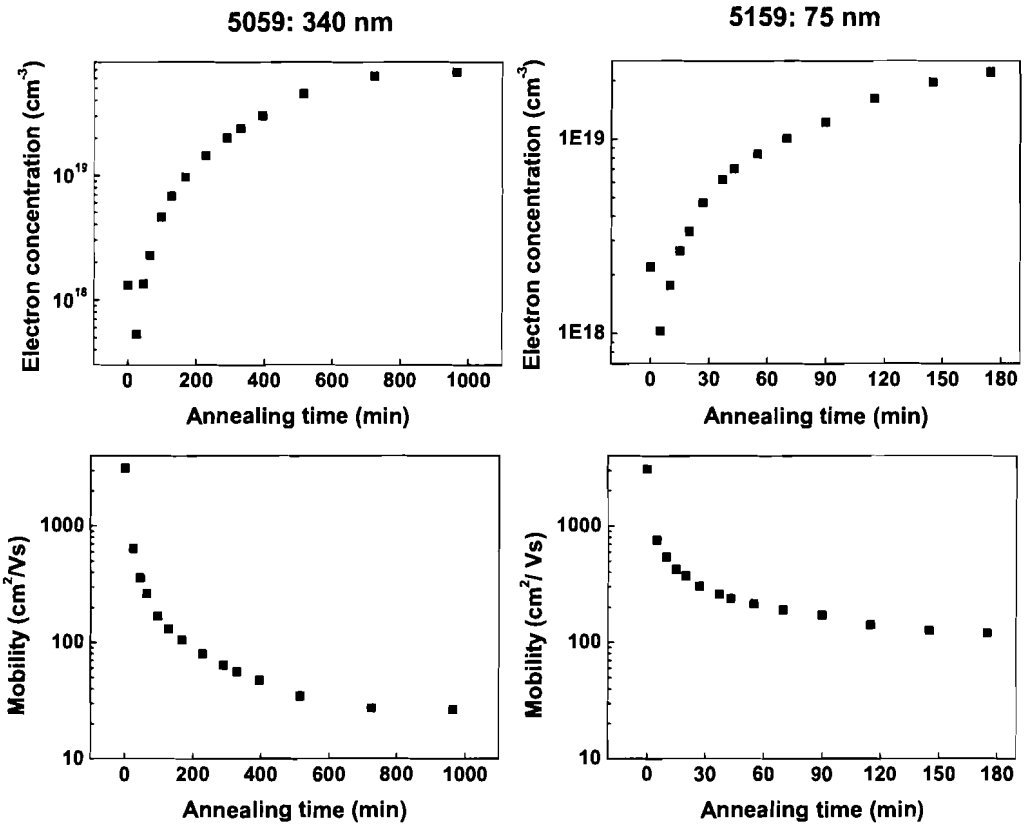

Figure 4.6: The electron concentration and the mobility of the samples annealed at 400 °C in a N_2 ambient.

4.4 Energy level of dicarbon defects in InAs

In contrast to the shallow impurities that are usually produced by the long-ranged Coulomb potentials and their electron wave functions extend over several primitive cells, deep defects are formed by central cell, short-ranged potentials and have more localized electron wave functions. This is because of the large ionization energy of these levels that results in a strong potential [84]. Deep defects cannot be treated by effective mass approximation (like shallow defects), because their potential is not slowly varying in space.

The energy level of the shallow impurities usually lies within 0.1 eV from the conduction or valence band edges [85]; however, deep defects have energy levels deep inside the gap. Determining the energy level of a deep defect in a semiconductor material requires a knowledge of the potential of the defect and also a way to solve the related Schrodinger equation [86]. Calculating the defect potential is not an easy task considering that lattice relaxation can happen around the impurity.

In the case of shallow impurities the energy level is always close to the valence or conduction band edges, whereas this is not the case for deep defects. In the case of transition metal impurities, it has been found that there is not always a strong tie between the deep defect level and the band edges of the host crystal [87, 88]. There is a universal energy reference level that these deep levels can be referred to using a simple universal relation. One explanation for this is the lack of a strong interaction between the impurity and the host semiconductor.

As we mentioned before, theoretical calculations revealed that split interstitial dicarbon defects are deep donors in GaAs and have an energy level close to the midgap [72]; however the exact energy level was not mentioned. We made an estimation for the energy level of these defects in InAs and InP using the approximate energy level of the defect in GaAs and the fact that the energy level of deep defects is not strongly dependent on the host lattice. Figure 4.7 shows the results.

The energy values have been calculated using the model-solid approach by Van de Walle [89]. The absolute values of these levels do not have any physical meanings and they can only be used for comparison with similar quantities in other materials.

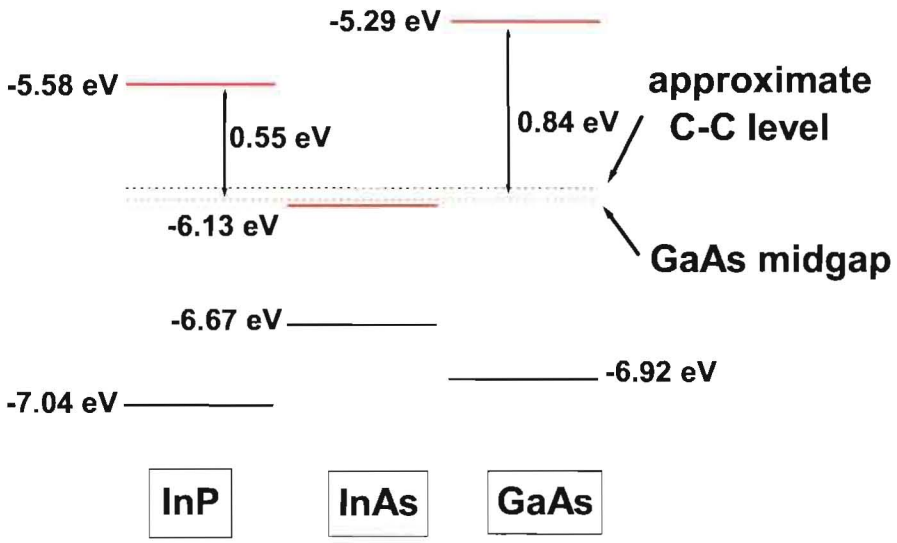

Figure 4.7: The band line up and the approximate energy level of dicarbon defects in GaAs, InAs, and InP. Conduction bands are shown by solid red lines and the valence bands are shown by solid black lines.

According to this graph, the energy level of dicarbon defects in InP should lie deep inside the gap; however, for InAs it should lie close to or slightly above the conduction band minimum and become a resonant state [86]. Resonant states form when the energy level of a deep defect overlaps with the band states of the host. Since the energy level lies outside the gap, conventional methods such as deep level transient spectroscopy (DLTS) cannot be used for detection. Hydrostatic pressure is commonly used to force the energy level inside the energy gap by changing the relative energies of the band edges [90]. Kadri *et al.* detected a resonant deep donor level for n-type InAs by applying high hydrostatic pressures that resulted in the downward shift of the level and consequently the carrier freezeout into this level [91]. A similar approach can be used in the future to investigate the dicarbon level in InAs:C.

The preceding arguments indicate that dicarbon should introduce a level near or

slightly above the conduction band minimum. Such a level should be expected to always act as a shallow donor of electrons. Freezeout would not be expected except for very low temperatures and carbon concentrations. Temperature dependent Hall measurements were conducted on some samples and the results are presented in the following section. No carrier freezeout was observed for these samples. Therefore, our Hall data do not allow us to state exactly where the dicarbon level lies.

4.5 Temperature dependent Hall measurements of InAs:C

Early on in the thesis we speculated that dicarbon might be a deep level donor defect. In order to investigate this possibility, temperature dependent Hall measurements were conducted on 2-micron thick undoped and low carbon doped InAs samples in the temperature range of 8 K to 290 K. Figure 4.8 shows the electron concentration and the mobility of the n-type, undoped and carbon-doped samples. The electron concentration of both samples showed a very slight change with temperature. No carrier freezeout was observed for these samples. The behaviour of the undoped sample is well understood. InAs exhibits an accumulation layer at the surface due to the pinning of the surface Fermi level above the conduction band edge. The electrical transport of InAs happens in two layers: the surface accumulation layer and the bulk layer. The carrier mobility of the surface layer is lower than that of the bulk layer due to the higher electron concentration. The mobility of the bulk layer is the result of competition between two scattering mechanisms: lattice scattering and ionized impurity scattering [92]. In the low temperature region, it increases with increasing temperature and, after reaching a peak value, it drops due to the scattering of electrons by lattice phonons. Because of the high mobility of the bulk layer in the low temperature region, this layer has the dominant role in the conduction. The rather low variation in the measured sheet electron concentration can be attributed to the more dominant role of the surface accumulation layer in the sheet concentration. It has been shown ([93]) that this kind of conduction is dependent on the sample thickness.

The relatively low variation in the mobility and the sheet concentration is due to the low thickness of the samples. For the doped sample, very little change is observed in either the mobility or the carrier concentration. This must be interpreted as being due to a very high level of bulk donor conduction. The data show no evidence of freezeout, however this is not necessarily proof that the dicarbon level is not inside the forbidden gap. At these high doping levels, degenerate conduction would still be expected for a level inside the forbidden gap. However, our energy level argument places the dicarbon level close to or above the conduction band minimum. In any case the observed Hall data are consistent with expectation.

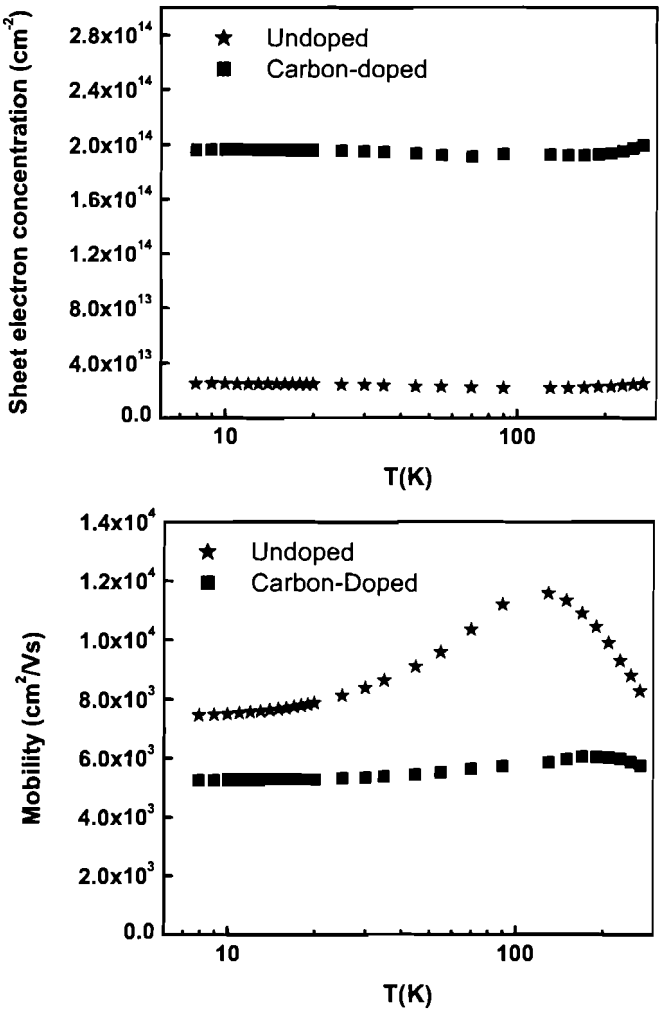

Figure 4.8: Electron concentration and mobility of 2-micron thick undoped and carbon-doped InAs samples as a function of temperature.

4.6 LVM spectroscopy of carbon-doped GaSb

The first carbon doping of OMVPE-grown GaSb has been reported by our group [94]. It has been shown that a hole concentration greater than 10^{19} cm^{-3} can be easily achieved for this material with very low hydrogen passivation. Local vibrational modes at 540 cm^{-1} were detected for the C-doped GaSb and were attributed to carbon acceptors substituting for Sb lattice sites in comparison with carbon-doped GaAs [2]. Another line at 167 cm^{-1} was detected in Raman spectra of the doped material and was assigned as the gap mode of the carbon acceptors. To our knowledge there is no report of hydrogen passivation of carbon acceptors in GaSb.

In this section, we confirm the assignment of the previously detected LVM at 540 cm^{-1} to the substitutional carbon acceptors using the isotopic shift of this LVM. We'll also report the results of our search for the carbon-hydrogen complexes and discuss the possible reasons for the difficulty of passivating carbon acceptors with hydrogen in this compound.

4.6.1 Isotopic shift of the carbon LVMs in GaSb

We conducted Raman spectroscopy measurements on two sets of samples: one doped with natural carbon (99 % ^{12}C) and the other doped with both isotopes of carbon (70 % ^{13}C and 30 % ^{12}C). Measurements were conducted at the temperature of 15 K using the 514 nm line of an Ar^+ laser. Figure 4.9 (a) shows the spectra in the frequency range of 100 to 600 cm^{-1} and (b) is a blow up of the carbon region. In addition to the previously detected LVM at 540 cm^{-1} , another line appears at the wavenumber of 521 cm^{-1} . The square of the ratio of the wavenumbers, $(^{12}\omega/^{13}\omega)^2$=1.074, is very close to the ratio of the atomic weights of two isotopes (13/12=1.083). The ratio of the intensities of these two lines is 2.8 close to the ratio of the abundances of two isotopes in the carbon source. All these data show that the lines are related to an isolated carbon defect.

The mass defect model (equation 2.18) can be used to indicate the lattice site of the carbon defects. Replacing the nearest neighbor mass (M_{NN}) with the Sb and Ga atomic masses gives the values of 0.87 and 1.52, respectively, for χ. The second

value is very close to the typical value of 2 for the χ parameter. Therefore it can be concluded that carbon atoms occupy the Sb lattice sites in this material and become acceptors as expected from the strong tendency to form p-type material.

There is a weak line at the wavenumber of 161 cm^{-1} in the Raman spectra of both samples (figure 4.9(a)). Chen *et al.* [2] have reported the detection of a LVM at 164 cm^{-1} and attributed that to the carbon gap mode according to the theoretical predictions of Robbie *et al.* [21]. As can be seen in figure 4.9(a), this peak appears at the same frequency for both samples and no isotopic shift was observed. It has been observed for other materials that the isotopic shift of the gap modes are much smaller than those of the LVMs. For example, the isotopic shift of the gap mode of B_{Ga} in GaP ($\sim$1 cm^{-1}) is 10 times smaller than that of the corresponding LVM [95]. They have attributed this to the fact that these modes are more extended than LVMs and impurity isotopic shifts are smaller than those of LVMs. Therefore high resolution measurements are needed to detect any possible shift. The assignment of this line to the gap modes of carbon defects can not be rejected.

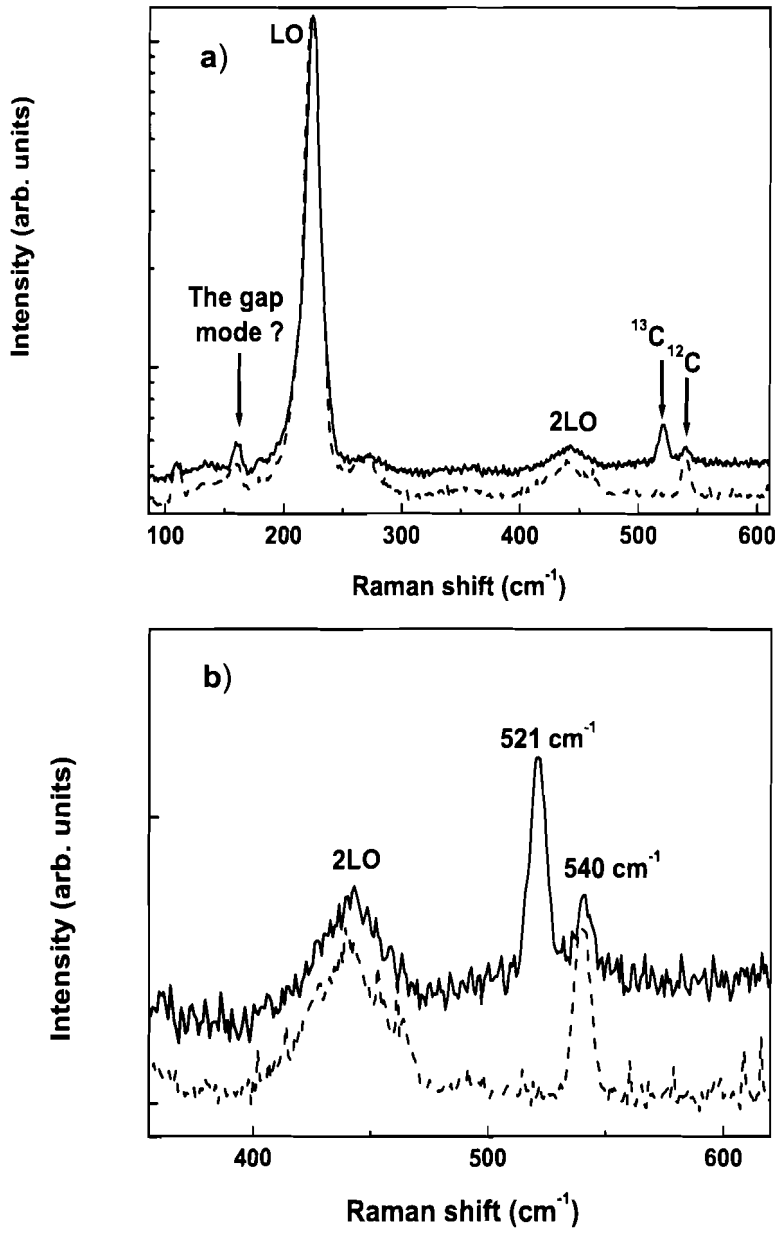

Figure 4.9: a) Raman spectra of GaSb samples doped with natural carbon (dashed line) and a mixture of carbon isotopes with the abundance ratio of $^{13}C/^{12}C$=70/30 (solid line), b) carbon region of the spectra.

4.6.2 Hydrogen passivation of carbon acceptors in GaSb

FTIR reflectivity measurements had been previously conducted by our group on different carbon-doped GaSb samples to study the hydrogen passivation of carbon acceptors in this material. Several as-grown samples with different hole concentrations and one hydrogen plasma-treated sample were used for the measurements. We repeated these measurements on the same samples and reproduced most of the previous results. Figure 4.10 shows some of these FTIR reflectance spectra.

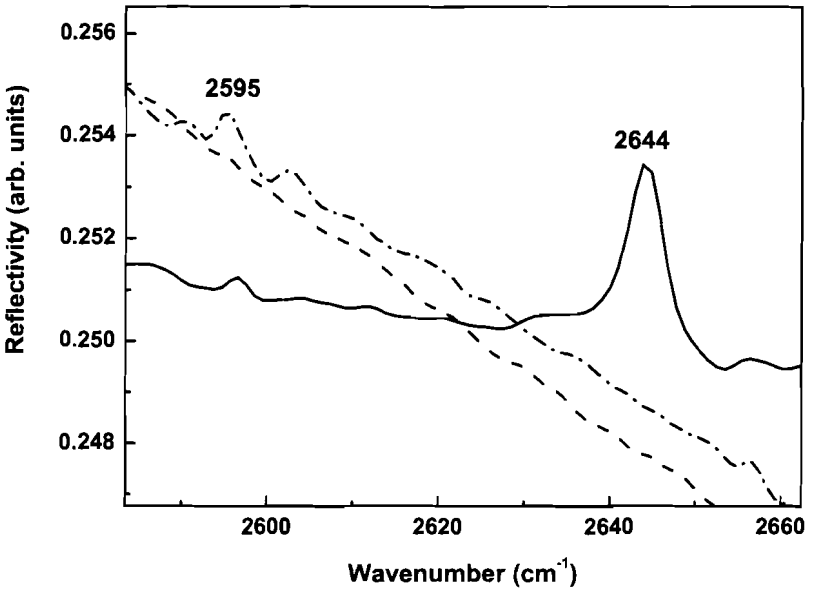

Figure 4.10: IR reflectance spectra of the as-grown samples with p=7.90×10^{19} cm^{-3} (dash-dot line), p=1.20×10^{19} cm^{-3} (dashed line), and the second one treated by H-plasma (solid line).

There are two main features in the spectrum of the hydrogen plasma-treated sample: one strong line at the wavenumbers of 2644 cm^{-1} and another weak line at 2595 cm^{-1} . None of these peaks were detected for the same sample before H-plasma treatment; however the line at 2595 appeared on the spectra of some other as-grown

samples (one is shown on the figure). Considering that the strong line was not detected for any of the as-grown samples, we suspect that it may be related to the contamination of the surface of the sample. On the other hand, the frequency of the weak line at 2595 cm^{-1} fits very well on the trend of C-H LVM frequency vs lattice constant as shown in figure 4.11. Although there is no direct evidence showing that

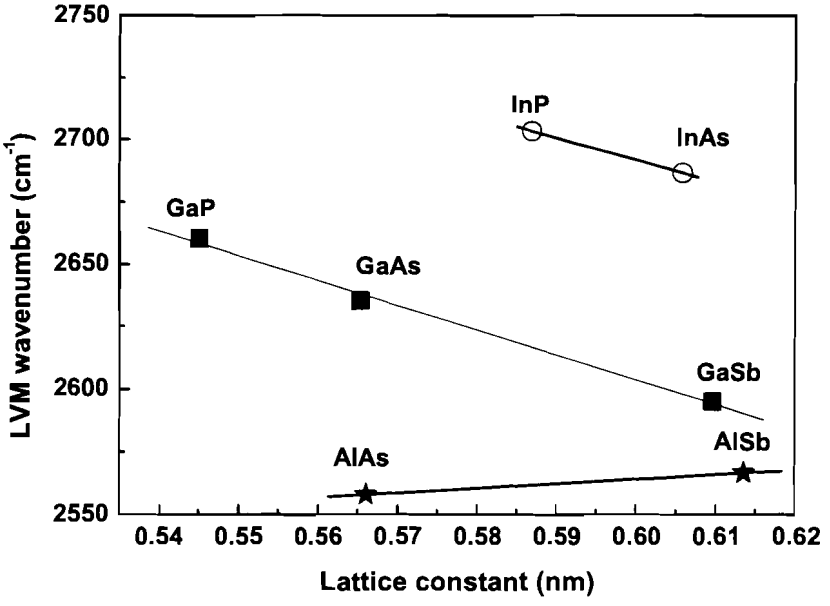

Figure 4.11: Frequency of C-H LVMs of different semiconductors vs their lattice constants.

this peak is the stretch mode of the C-H complex in GaSb, its presence on the IR spectra of some samples and also its frequency value strengthens the possibility of assigning this line to C-H stretch mode.

IR absorption measurements were performed on several highly doped samples but they did not reveal any peak in this frequency range. We examined the effect of the substrate temperature on the hydrogen passivation of carbon acceptors by doing IR absorption measurements on samples grown at substrate temperatures of 550, 500,

and 460 °C. C-H related LVMs could not be detected for any of these samples. It is not still clear why we could not detect the previously observed lines on FTIR reflectance spectra by IR absorption measurements. One possible explanation would be the very low concentration of these defects in GaSb due to the difficulty of passivating the carbon acceptors of GaSb and GaAsSb [96] (The reason is not known yet). Therefore the exact assignment of the peak at 2595 cm^{-1} to a C-H stretch mode requires careful IR reflectance measurements on several samples doped with both isotopes of carbon. Nevertheless, the difficulty of creating C-H pairs is good news for device work.

Chapter 5

Conclusions

Carbon doping of InAs and GaSb samples grown by OMVPE method was investigated. Electrical, structural, and vibrational properties of InAs:C samples were studied using SIMS measurements, Hall measurements, XRD, Raman spectroscopy, and IR absorption measurements. The origin of n-type conductivity of InAs:C was investigated.

It was found that incorporation of carbon is strongly dependent on the growth temperature. SIMS results showed that incorporation of carbon increases significantly by decreasing temperature lower than 400 °C. These results also revealed the presence of hydrogen in all samples. Concentration of hydrogen atoms was correlated with that of carbon atoms and depended on the growth temperature.

Hall measurements showed that carbon doped samples have n-type conductivity. Electron concentration increased by lowering growth temperature and was correlated with CBr_4 flow rate. This indicated that n-type conductivity of samples originates from carbon related donors. According to XRD patterns, carbon doping of InAs reduced the lattice constant of this material.

Local vibrational modes of carbon and carbon-hydrogen complexes and their isotopical shifts were detected by Raman and IR spectroscopy methods. LVMs of ^{12}C detected at 530 cm^{-1} with isotopical shift of 19 cm^{-1} was attributed to isolated carbon atoms occupying the As lattice sites. Detection of three different modes of C-H complexes at 393.2, 518.2, and 2686.2 cm^{-1} showed that passivating hydrogen atoms

occupy bond center position between C and In atoms and this is in agreement with the presence of isolated carbon atoms at group V lattice sites. In addition to carbon and C-H LVMs, local vibrational modes of of substitutional C-C complexes were also detected at 1832 cm^{-1} by Raman spectroscopy in as-grown InAs:C samples.

Thermal stability of carbon doped InAs samples was studied by annealing the samples at temperatures of 400°C and higher. It was found that annealing increased the lattice constant of doped samples towards that of undoped samples. Raman and IR spectroscopy results showed that concentration of carbon and carbon-hydrogen complexes reduced dramatically by annealing. This was accompanied by an increase in the concentration of dicarbon centers.

Considering all these observations we concluded that carbon occupies the group V lattice site in InAs similar to other III-V semiconductors. Due to lower bond strength between carbon and In, the stability of carbon is lower than that in other materials. Therefore, it can easily diffuse out of group V lattice sites and forms dicarbon complexes with other substitutional carbon atoms. These complexes have shown to be donors in GaAs and InP. The n-type conductivity of InAs:C samples is due to high concentrations of these defects.

Carbon doping and hydrogen passivation of carbon atoms in GaSb were studied by Raman and IR spectroscopy methods. The assignment of previously determined LVM at 540 cm^{-1} to isolated carbon acceptors was confirmed measuring the isotopic shift of this line. No C-H defects were detected in as-grown and annealed carbon doped GaSb samples. More theoretical investigation is needed to explain the difficulty of passivating carbon atoms by hydrogen in this material.

Bibliography

[1] M. R. Brozel, R. C. Newman, and J. B. Clegg. *J. Phys. D*, 11(9):1331, (1978).

[2] X. K. Chen, R. Wiersma, C. X. Wang, O. J. Pitts, C. Dale, C. R. Bolognesi, and S. P. Watkins. *Appl. Phys. Lett*, 80(11):1942, (2002).

[3] B. R. Davidson, R. C. Newman, D. A. Robbie, M. J. L. Sangster, J. Wagner, A. Fischer, and K. Ploog. *Semicond. Sci. and Technol.*, 8(4):611, (1993).

[4] C. R. Abernathy. *Appl. Phys. Lett.*, 55(17):1750, (1989).

[5] S. A. Stockman, A. W. Hanson, and G. E. Stillman. *Appl. Phys. Lett.*, 60(23):2903, (1992).

[6] M. Kamp, R. Contini, K. Werner, H. Heinecke, M. Wyers, H. Luth, and P. Balk. *J. Cryst. Growth*, 95:154, (1989).

[7] W. Schoenfeld, M. J. Antonell, and C. R. Abernathy. *J. Cryst. Growth*, 188:50, (1998).

[8] H. Ito and T. Ishibashi. *Jpn. J. Appl. Phys.*, 30(6A):L944, (1991).

[9] M. Kamp, M. Weyers, H. Heinecke, H. Lüth, and P. Balk. *J. Cryst. Growth*, 105:178, (1990).

[10] K. J. Chang, S. G. Lee, and B. H. Cheong. *Materials Science Forum*, 196-201:803, (1995).

[11] S.P. Watkins, R.D. Wiersma, C.X. Wang, O.J. Pitts, and C.R. Bolognesi. *J. Cryst. Growth.*, 248:274, (2003).

[12] G. B. Stringfellow. *Organometallic vapor-phase epitaxy: Theory and Practice.* Academic Press, (1999).

[13] M. A. Herman, W. Richter, and H. Sitter. *Epitaxy, Physical Principles and Technical Implementation.* Springer, (2004).

[14] Z. G. Pinsker. *Dynamical scatering of X-rays in crystals.* Springer, (1978).

[15] M. Leszczynski, J. Bak-Misiuk, J. Domagala, J. Muszalski, M. Kaniewska, and J. Marczewski. *Appl. Phys. Lett.*, 67(4):539, (1995).

[16] A. Krost, G. Bauer, and J. Woitok. *Optical characterization of epitaxial semiconductor layers.* Springer, (1996).

[17] Daniel M. Boerger, John J. Kramer, and Larry D. Partain. *J. of Appl. Phys.*, 52(1):269–274, 1981.

[18] V. P. Tolstoy, I. V. Chernyshova, and V. A. Skryshevsky. *Handbook of infrared spectroscopy of ultrathin films.* Wiley-interscience, (2003).

[19] A. S. Barker and A. J. Sievers. *Rev. Mod. Phys.*, 47:S1, (1975).

[20] A. A. Maradudin, E. W. Montroll, C. H. Weiss, and I. P. Ipotova. *Solid State Physics.* Academic, New York, second edition, (1971).

[21] D. A. Robbie, M. J. L. Sangster, and P. Pavone. *Phys. Rev. B*, 51:10489, (1995).

[22] M. Stavola, editor. *Semiconductos and Semimetals*, volume 51B. Academic Press, INC., New York, (1999).

[23] R.C. Newman. *Adv. Phys.*, 18(75):545, (1969).

[24] E. R. Weber, editor. *Semiconductos and Semimetals*, volume 38. Academic Press, INC., New York, (1993).

[25] M. D. McCluskey. *J. Appl. Phys.*, 87(8):3593, (2000).

[26] R. S. Leigh and R. C. Newman. *Semicond. Sci. Technol.*, 3(6A), (1988).

[27] B. R. Davidson, R. C. Newman, and C. C. Button. *Phys. Rev. B*, 58(23):15609, (1998).

[28] N. Esser and J. Geurts. *Optical characterization of epitaxial semiconducto layers.* Springer, (1996).

[29] W. G. Fateley, F. R. Dollish, N. T. McDevitt, and F. F. Bentley. *Infrared and Raman selection rules for molecular and lattice vibrations.* Wiley-interscience, (1972).

[30] M. Cardona. *Light scattering in solids II.* Springer, (1982).

[31] R. Merlin, A. Pinczuk, and W. H. Weber. *Raman scattering in materials science.* Springer, (2000).

[32] J. C. Tsang, K. Eberl, S. Zollner, and S. S. Iyer. *Appl. Phys. Lett.*, 61:961, (1992).

[33] S. J. Pearton, U. K. Chakrabarti, C. R. Abernathy, , and W. S. Hobson. *Appl. Phys. Lett.*, 55:2014, (1989).

[34] S. A. Stockman, M. T. Fresina, Q. J. Hartmann, A. W. Hanson, N. F. Gardner, J. E. Baker, and G. E. Stillman. *J. Appl. Phys.*, 75(8):4233, (1994).

[35] B. Theys, J. L. Benchimol, E. V. K. Rao, J. Chevallier, and M. Juhel. *Appl. Phys. Lett.*, 72(20):2568, (1998).

[36] M. Ramsteiner and P. Kleinert. *Appl. Phys. Lett.*, 67(5):647, (1995).

[37] R. C. Newman, B. R. Davidson, R. S. Leigh, M. J. L. Sangster, and C. C. Button. *Physica B*, 273-274:827, (1999).

[38] R.C. Newman, B.R. Davidson, J. Wagner, M.J.L. Sangster, and R.S. Leigh. *Phys. Rev. B*, 63:205307, (2001).

[39] J. Wagner, R. C. Newman, B. R. Davidson, S. P. Westwater, T. J. Bullough, T.B. Joyce, C.D. Latham, R. Jones, and S. Oberg. *Phys. Rev. Lett.*, 78(1):74, (1997).

[40] Byoung-Ho Cheong and K. J. Chang. *Phys. Rev. B*, 49(24):17436, (1994).

[41] M. J. Begarney, M. L. Warddrip, M. J. Kappers, and R. F. Hicks. *J. Cryst. Growth*, 193:305, (1998).

[42] N. I. Buchan, T. F. Kuech, G. Scilla, and F. Cardone. *J. Cryst. Growth*, 110:405, (1991).

[43] N. F. Gardner, Q. J. Hartmann, J. E. Baker, and G. E. Stillman. *Appl. Phys. Lett.*, 67(20):3004, (1995).

[44] Je-Hwan Oh and Jun ichi Shirakashi. *Appl. Phys. Lett.*, 66(21):2891, (1995).

[45] M. C. Hanna, Z. H. Lu, and A. Majerfeld. *Appl. Phys. Lett.*, 58(2):164, (1991).

[46] Y. Oda, N. Watanabe, H. Yokoyama, and T. Kobayashi. *Appl. Surf. Sci.*, 216(1-4):532, (2003).

[47] T. J. de Lyon, J.M. Woodall, M. S. Goorsky, and P.D. Kirchner. *Appl. Phys. Lett.*, 56(11):1040, (1990).

[48] Y. B. Li, I. T. Ferguson, R. A. Stradling, and R. Zallen. *Semicond. Sci. Technol.*, 7:1149, (1992).

[49] J. Wagner, P. Koidl, and R. C. Newman. *Appl. Phys. Lett.*, 59(14):1729, (1991).

[50] S. Buchner and E. Burstein. *Phys. Rev. Letts.*, 33(15):908, (1974).

[51] B. R. Davidson, R. C. Newman, T. J. Bullough, and T. B. Joyce. *Phys. Rev. B*, 48(23):17106, (1993).

[52] V. J. B. Torres, J. Coutinho, and P. R. Briddon. *Physica B*, 401-402:275, (2007).

[53] J. Chevallier, B. Clerjaud, and B. Pajot. *Semiconductos and Semimetals*, volume 34. Academic Press, INC., New York, (1991).

[54] S. J. Pearton, J. W. Corbett, and M. Stavola. *Hydrogen in crystalline semiconductors.* Springer-Verlag, Berlin ; New York, (1992).

[55] C. G. Van de Walle and J. Neugebauer. *Nature*, 423:626, (2003).

[56] H. P. Gislason. *Physica Scripta.*, T69:40, (1997).

[57] N. M. Johnson, R. D. Burnham, R. A. Street, and R. L. Thornton. *Phys. Rev. B*, 33(2):1102, (1986).

[58] S. J. Pearton, W. S. Hobson, and C. R. Abernathy. *Phys. Rev. B*, 61(13):1588, (1992).

[59] C. R. Abernathy, J. D. MacKenzie, W. S. Hobson, and P. W. Wisk. *Appl. Phys. Lett.*, 65(17):2205, (1994).

[60] B. Clerjaud, F. Gendron, M. Krause, and W. Ulrici. *Phys. Rev. Lett.*, 65(14):1800, (1990).

[61] J. Wagner, R. E. Pritchard, B. R. Davidson, R. C. Newman, T. J. Bullough, T. B. Joyce, C. Button, and J. S. Roberts. *Semicond. Sci. Technol.*, 10(5):639, (1995).

[62] R. Jones and S. Öberg. *Phys. Rev. B*, 44(8):3673, (1991).

[63] D. M. Kozuch, Michael Stavola, S. J. Pearton, C. R. Abernathy, and W. S. Hobson. *J. Appl. Phys.*, 73(8):3716, (1993).

[64] Ying Cheng, Michael Stavola, C. R. Abernathy, S. J. Pearton, and W. S. Hobson. *Phys. Rev. B*, 49(4):2469, (1994).

[65] K. J. Chang and D. J. Chadi. *Phys. Rev. B*, 40(17):11644, (1989).

[66] J. Vetterhöffer and J. Weber. *Phys. Rev. B*, 53(19):12835, (1996).

[67] B. Pajot, R. C. Newman, R. Murray, A. Jalil, J. Chevallier, and R. Azoulay. *Phys. Rev. B*, 37(8):4188, (1988).

[68] M. J. Ashwin, M. R. Fahy, R. C. Newman, J. Wagner, D. A. Robbie, M. J. L. Sangster, E. Bauser I. Silier, W. Braun, and K. Ploog. *J. Appl. Phys.*, 76(12):7839, (1994).

[69] B. R. Davidson, R. C. Newman, T. Kaneko, and O. Naji. *Phys. Rev. B*, 50(16):12250, (1994).

[70] B. R. Davidson, R. C. Newman, H. Fushimi, K. Wada, H. Yokoyama, and N. Inoue. *J. Appl. Phys.*, 81(11):7255, (1997).

[71] S.P. Westwater and T.J. Bullough. *J. Crys. Growth*, 170:752, (1997).

[72] R. Jones and S. Oberg. *Materials Science Forum*, 143(1):253, (1994).

[73] B.R. Davidson, R.C. Newman, C.D. Latham, R. Jones, J. Wagner, C.C. Button, and P.R. Briddon. *Phys. Rev. B*, 60(8):5447, (1999).

[74] K. Watanabe and H. Yamazaki. *Appl. Phys. Lett.*, 59(4):434, (1991).

[75] P. Enquist. *J. Appl. Phys.*, 71(2):704, (1992).

[76] S.P. Westwater and T.J. Bullough. *J. Cryst. Growth*, 170(1):752, (1997).

[77] J. D. MacKenzie, C. R. Abernathy, S. J. Pearton, and S. N. G. Chu. *Appl. Phys. Lett.*, 66(11):1397, (1995).

[78] A. Tandon and R.M. Cohen. *J. Cryst. Growth.*, 192(1-2):47, (1998).

[79] J. Mimila-Arroyo, A. Lusson, J. Chevallier, M. Barbe, B. Theys, F. Jomard, and S.W. Bland. *Appl. Phys. Lett.*, 79(19):3095, (2001).

[80] W. Li and M. Pessa. *Phys. Rev. B*, 57(23):14627, (1998).

[81] N. Chen, Y. Wang, H. He, and L. Lin. *Phys. Rev. B*, 54(12), (1996).

[82] W.Y. Han, Y. Li, H.S. Lee, M.W. Cole, S.N. Schauer, R.P. Moerkirk, K.A. Jones, and L.W. Yang. *Appl. Phys. Lett.*, 61(1):87, (1992).

[83] G. B. Stringfellow and H. Kunzel. *Phys. Rev. B*. 51(6):3254, (1980).

[84] P. M. Mooney. *Identification of defects in semiconductors.* Academic press, (1999).

[85] C. M. Myles and O. F. Sankey. *Phys. Rev. B*, 29(12):6810, (1984).

[86] P. Y. Yu and M. Cardona. *Fundamentals of semiconductors.* Springer, Berlin, (1996).

[87] M. J. Caldas, A. Fazzio, and A. Zunger. *Appl. Phys. Lett.*, 45:671, (1984).

[88] H. Hasegawa. *Solid State Communications*, 58:157, (1986).

[89] Chris G. Van de Walle. *Phys. Rev. B*, 39(3):1871, (1989).

[90] A. K. Saxena and P. Singh. *Phys. Stat. Sol. (b)*, 195:451, (1996).

[91] A. Kadri, R. L. Aulombard, K. Zitouni, M. Baj, and L. Konczewicz. *Phys. Rev. B*, 31(12):8013, (1985).

[92] B. Streetman and S. Banerjee. *Solid state electronic devices.* Prentice Hall, (2000).

[93] S. P. Watkins, C. A. Tran, R. Ares, and G. Soerensen. *Appl. Phys. Lett.*, 66(7), (1995).

[94] R. Wiersma, J.A.H. Stotz, O.J. Pitts, C.X. Wang, M.L.W. Thewalt, and S.P. Watkins. *Journal of Electronic Materials*, 30(11), (2001).

[95] E. G. Grosche, M. J. Ashwin, R. C. Newman, D. A. Robbie, M. J. L. Sangster, T. Pletl, P. Pavone, and D. Strauch. *Phys. Rev. B*, 51(20):14758, (1995).

[96] Y. Oda, N. Watanabe, M. Uchida, K. Kurishima, and T. Kobayashi. *J. Cryst. Growth.*, 272:700, (2004).